INVESTIGATING THE INFLUENCE OF MICROSTRUCTURE ON CORROSION SUSCEPTIBILITY: A MULTISCALE ELECTRON MICROSCOPY APPROACH

A Dissertation
Presented to
The Academic Faculty

by

Jordan W. Key

In Partial Fulfillment
of the Requirements for the Degree
Doctorate of Philosophy in the
School of Materials Science and Engineering

Georgia Institute of Technology
May 2020

INVESTIGATING THE INFLUENCE OF MICROSTRUCTURE ON CORROSION SUSCEPTIBILITY: A MULTISCALE ELECTRON MICROSCOPY APPROACH

Approved by:

Dr. Josh Kacher, Advisor
School of Materials Science and Engineering
Georgia Institute of Technology

Dr. Matthew McDowell
School of Materials Science and Engineering
Georgia Institute of Technology

Dr. Preet Singh
School of Materials Science and Engineering
Georgia Institute of Technology

Dr. Andrew Medford
School of Chemical and Biomolecular Engineering
Georgia Institute of Technology

Dr. Hamid Garmestani
School of Materials Science and Engineering
Georgia Institute of Technology

Date Approved: March 23, 2020

To myself, for overcoming the self-doubt and seeing it through to the end

ACKNOWLEDGEMENTS

There are many people to whom I owe an enormous debt of gratitude for their kindness and support throughout this process. First, I would like to thank Dr. Josh Kacher for his continued support and encouragement as my advisor. Josh is a great person to work for, and he has many creative and exciting ideas of how to keep materials science research on the cutting edge. His guidance and aid were critical to help me see this through to the end. I would also like to thank the rest of my committee: Dr. Preet Singh, Dr. Matthew McDowell, Dr. Hamid Garmestani, and Dr. Andrew Medford. They took time out of their busy schedules to provide feedback and advice on my dissertation work, ensuring that it was well-rounded and thorough. I would also like to thank all the collaborators that I worked with over the years, including Dr. Raymond Unocic, Dr. Christopher Rouleau, and Dr. Yao Xi. They were each passionate and kind in their interactions with me, and they did their best to use their extensive expertise to help me succeed.

I also want to thank the members of the Kacher Lab at Georgia Tech, particularly Jeremy Yoo. Jeremy and I were Josh's first students and we helped him build the lab from the beginning. Throughout the last five years we have supported each other, commiserated together, congratulated each other, and helped ensure that the other was going to make it through to the end. I would also like to thank the rest of the Kacher Lab, including Jahnavi, Pragna, Katie, Sandra, and Rupesh. They each contributed in their own way to my success, whether by assisting in experimentation, discussing project design, or providing feedback on presentations. I know the future of the lab will be bright with all of you to carry the torch. I would also like to thank Dr. Mengkun Tian for his support with instrumentation

and being willing to use his microscopy expertise to assist me whenever I needed it. I would also like to thank Dr. Yong Ding, Eric Woods, and Todd Walters for their companionship and advice while I used the IEN facilities. It was great getting to know them all and see them as role models in a shared-user research environment.

Finally, on a more personal level, I would like to thank all of my friends and family for their constant support throughout this long journey. Many fellow grad students, both at Georgia Tech and at other schools, were part of a support network that made this challenge much more bearable. Game nights and D&D sessions and many other social activities helped us all keep our sanity. I would like to thank those who came before that gave me advice, especially my peer mentor (now Dr.) Chris Perini. From my first day at Tech, Chris was a warm and enthusiastic presence that made our department feel more like home. I'd especially like to thank my sister, my parents, and my other family members for encouraging me, as well as my friends from across the country who I know through cosplay. I thank each and every one of you for your encouragement and support. But most of all I'd like to thank my wife Kat, for being a constant rock and support for me our entire marriage. Her love is sustaining and strengthening, and she supports me so much while also working on her own degree. She's a rock star and has started a wonderful new career and will soon be wrapping up a dissertation of her own. I'm very proud of her.

TABLE OF CONTENTS

LIST OF TABLES

LIST OF FIGURES

LIST OF SYMBOLS AND ABBREVIATIONS

P-S-P	Processing-Structure-Property
EBSD	Electron Backscatter Diffraction
LC-TEM	Liquid Cell Transmission Electron Microscopy
SEM	Scanning Electron Microscopy
AA5083	Aluminum Association 5083
TEM	Transmission Electron Microscopy
GND	Geometrically Necessary Dislocation
EDS	Energy Dispersive (X-Ray) Spectroscopy
IPF	Inverse Pole Figure
r_a	Anodic Dissolution Rate
K_2	Proportionality Constant for Anodic Dissolution
A_c / A_A	Cathode-to-Anode Area Ratio
IGC	Intergranular Corrosion
E_{pp}	Pitting Potential
i_c	Critical Current Density
E_{prot}	Protection Potential
E_r	Repassivation Potential
ECAP	Equal Channel Angular Pressing
i_{corr}	Corrosion Current Density
gs	Grain Size
PFZ	Precipitate Free Zone
SE	Secondary Electron

BSE	Backscattered Electron
Z	Atomic Number
AES	Auger Electron Spectroscopy
α	Nye Dislocation Density Tensor
κ	Curvature
ε^{el}	Elastic Strain
CDF	Centered Dark Field
BF	Bright Field
STEM	Scanning Transmission Electron Microscopy
EELS	Electron Energy Loss Spectroscopy
CI	Confidence Index
NAMLT	Nitric Acid Mass Loss Testing
CCD	Charge Coupled Device
CMOS	Complementary Metal-Oxide-Semiconductor

SUMMARY

In recent years, researchers have been leveraging developments in novel experimental methods and automated processing and analysis to establish processing-structure-property links in a more robust and statistical manner. One prime area that would benefit from such an approach is corrosion studies. Corrosion is an important societal issue with a broad and varied impact, and the corrosion-related maintenance and repair imposes a large expense on the global economy. This makes it important to better understand and predict corrosion behavior in order to design superior corrosion resistant materials. This work investigates the role of local microstructure in determining the corrosion behavior of materials, at the mesoscale and the nanoscale, through the combination of automated image processing and rapid, detailed characterization.

This work is divided into two parts. At the mesoscale, detailed microstructural characterization through SEM and EBSD analysis is combined with automated image processing to develop first order correlations between pit initiation and grain orientation, intermetallic particle proximity, grain boundary proximity, and local dislocation density in 5083 aluminum. At the nanoscale, *in situ* TEM oxidation investigations of Fe thin films are combined with automated image processing to track dynamic processes in real time. Information on oxidation front propagation behavior and kinetics, as well as crystallographic evolution, is extracted. These findings improve the understanding of the influence of microstructure on corrosion and lay the groundwork for further developments of these methodologies.

CHAPTER 1. INTRODUCTION AND MOTIVATION

One of the most fundamental tenets of materials science and engineering is the need to develop processing-structure-property (P-S-P) relationships. Fundamentally, a material's properties are determined by its structure (at many length scales, including the mesoscale and the nanoscale). The material's structure is a product of the processing path that was used to synthesize it. Different microstructural configurations have long been studied to determine how they affect material properties, and processing methods have been developed to manipulate that microstructure with an impressive amount of control. Materials scientists study the causal chains, the predictive links, between these different domains in the hope of turning them around and reverse engineering a recipe for the required material. This is the ultimate goal: to have in mind a set of material properties, to understand the microstructure needed to obtain these properties, and to know the processing path required to create that microstructure. Increasingly, researchers in recent years have been leveraging developments in technology to create these predictive P-S-P linkages. Two prominent advances include complex and novel experimental techniques and improved automated processing and analysis routines. These complex experimental techniques (i.e. *in situ* microscopy methodologies) enable rapid collection of rich datasets with high spatial and temporal resolution. Many of these improved automated analysis routines employ statistics, machine learning, neural networks, or some other data science method [1-5]. While both of these advancements are important in their own right, they also synergize with each other. This is because data-rich experimental techniques often need advanced automated analysis tools to extract the maximum amount of useful information.

A prime area that would greatly benefit from these technological developments is corrosion studies. Corrosion is an important societal issue with a broad and varied impact, ranging from plumbing infrastructure to naval vessels. Corrosion prevention and related maintenance is also quite expensive, costing the global economy an estimated $2.5 trillion annually [6]. This makes is particularly important to understand corrosion behavior and develop predictive P-S-P relations in order to facilitate the design of superior corrosion resistant materials that will reduce costs and increase safety. By combining rapid and powerful microstructural characterization methods with automated processing and analysis routines, great strides can be made towards such superior materials. In particular, electron backscatter diffraction (EBSD) analysis provides detailed microstructural characterization at the mesoscale including information on grain orientation, grain boundary character, and local dislocation density [7-9]. At the nanoscale, *in situ* liquid cell transmission electron microscopy (LC-TEM) provides direct observation of dynamic events in real time with high temporal and spatial resolution [10, 11]. These tools can provide a wealth of information on materials behavior, especially if used in combination with automated image processing and analysis routines. Image processing transforms qualitative electron microscopy imaging into quantitative data for statistical analysis. Scanning electron microscopy (SEM) imaging and EBSD analysis can be used to characterize relatively large areas (in mesoscale terms) relatively quickly, making them a good application for automated image processing that feeds into statistical analysis.

In this work, an automated image processing routine was used to extract pitting corrosion behavior from SEM imaging. The pit detection was combined with microstructural characterization by EBSD and statistical analysis to investigate first order

correlations between local microstructure and pitting initiation. This analysis framework was used to explore structure space in an Al-Mg alloy system by examining different microstructures and investigating the effects of various microstructural features on pitting. Creating this analysis toolbox lays the foundation for the rapid development of P-S-P relationships. This is because it enables rapid statistical analysis of multiple microstructural features, made possible through the combination of detailed characterization and automated image processing. The utility of this approach was established by investigating the 5083 aluminum alloy (AA5083) and correlating local microstructure to pitting initiation. Alternatively, this toolbox can be used to develop correlations for other materials systems and other forms of damage besides pitting corrosion, such as void nucleation in irradiated materials. At the nanoscale, *in situ* transmission electron microscopy (TEM) provides rich datasets of real-time information that are an ideal application for image processing and analysis that can track small changes in the system behavior. In this work, image processing was used to track propagation of oxidation events in an Fe system during *in situ* TEM experiments. This analysis extracted information about propagation rates and behavior that give important insight into the material response of the system. Again, such automated image processing methodologies can also be applied to other similar experimental systems. The core aspect of this approach is combining automated image analysis and statistical methods with rich experimental datasets. This work demonstrates the usefulness of such methods at both the mesoscale and nanoscale by developing analysis toolsets that are not only used to answer the specific problems in this work but can also be used to investigate other materials problems.

1.1 Objectives

The goal of this dissertation was to investigate the impact of microstructure on the pitting corrosion of the AA5083 system, to develop analysis toolsets or frameworks that can be used to develop P-S-P relations, and to enhance our understanding of dynamic corrosion processes including propagation behavior and kinetics. By combining rapid and/or rich characterization methods with automated image processing, statistical analysis can be leveraged to quickly develop predictive links. Although researchers have investigated the corrosion susceptibility of AA5083 for quite some time, there remain opportunities to improve our understanding by looking at the interplay of multiple microstructural features through multiscale experiments and the application of automated processing and analysis routines. The specific objectives for this work were to:

- Develop a materials agnostic analysis toolset for creating structure-property relations using a combination of mesoscale characterization, image processing, and statistical analysis
- Apply the above analysis toolset to develop correlations between pitting initiation and local microstructure in AA5083, specifically for grain orientation, intermetallic particle proximity, grain boundary proximity, and local geometrically necessary dislocation (GND) density
- Develop an analysis framework for extracting information from dynamic corrosion observations, such as corrosion behavior and kinetics, using *in situ* TEM and automated image analysis

To achieve these objectives, SEM imaging and EBSD microstructural characterization were employed to capture pitting initiation behavior in bulk samples and to correlate that initiation with key microstructural features in the system, namely crystallographic orientation, intermetallic particle proximity, grain boundary proximity, and local GND density. Automated image processing was used to create binary pitting maps that could be combined with microstructural maps extracted from EBSD using MATLAB scripts. Statistical analysis was then performed to determine the relative pitting frequency with respect to the various microstructural features. *In situ* LC-TEM experiments were also carried out on thin films and automated image processing methodologies were developed to track propagation behavior and kinetics, as well as to study crystallographic evolution of the system. Sequential image difference and thresholding were used to process high-frame-rate videos and quantify the reaction rates, as well as to compare different modes of reaction. Radial integration of diffraction patterns both individually and in aggregate provided identification of reaction byproducts. These tools can be utilized and further built upon by the community to continue to create predictive P-S-P relations and improve microstructure sensitive design.

1.2 Map of the Dissertation

This work improved the understanding of structure-property correlations for pitting initiation by developing an automated analysis toolset and applying it to the AA5083 system. This toolset can be used not only for pitting initiation of AA5083 but for other materials systems and other degradation mechanisms. This work also showed the

usefulness of *in situ* TEM methodologies in investigating dynamic corrosion events and highlighted the importance of automated analysis routines for processing rich *in situ* datasets. This section lays out a map of the dissertation in detail and shows how each chapter contributes toward the eventual accomplishment of the objectives outlined above.

In Chapter 2 I lay out the background needed to understand the materials problem to be addressed by this work and review the relevant literature regarding the impact of microstructure on corrosion. The primary modes of corrosion that are relevant to this work are galvanic corrosion, intergranular corrosion, and pitting corrosion. Each of these modes are impacted by various microstructural features such as grain size, grain boundary character, dislocation content, and secondary phase distribution. The available literature shows discrepancies that highlight the need to consider the interplay of multiple microstructural features with each other when investigating corrosion behavior. The literature specific to the sensitization and corrosion of AA5083 is reviewed, since it is the primary material system in this work and has its own specific challenges. Finally, the operating principles of the characterization methods used in this work, including SEM imaging, EBSD, energy dispersive x-ray spectroscopy (EDS), and LC-TEM are described. This chapter sets up the materials challenges that exist for the system in this work and describes the tools used to address them.

In Chapter 3 I detail the experimental parameters and approach used to investigate the corrosion behavior of the materials in this work. The mesoscale investigations are outlined, and a description is given for sample preparation and microstructure characterization of bulk AA5083. The experimental workflow used to obtain the microstructural features of interest is described, leading to the statistical analysis used to

generate correlations. Last is a discussion of the nanoscale investigations and description of the parameters used for the deposition of the Fe films, as well as the environmental conditions for the LC-TEM work.

In Chapter 4 I describe the development of the automated analysis toolset for creating mesoscale structure-property relations. SEM imaging is combined with EBSD to provide each microstructural feature of interest and programming scripts are used to generate microstructural maps for every region of interest. Crystallographic orientation, intermetallic particle proximity, grain boundary proximity, and local GND density are all investigated. Automated image processing is used to extract binarized pit maps from SEM imaging, and the workflow used in this processing is discussed. Finally, the results of these investigations are discussed for both sensitized and unsensitized AA5083 samples. Relative pitting histograms and inverse pole figures (IPFs) are generated showing the pitting behavior as a function of each microstructural feature. This chapter presents the design and specific application of the automated analysis toolset, demonstrating its usefulness in investigating structure-property relations.

In Chapter 5 I discuss the results of the nanoscale corrosion investigations and describe the automated image analysis used to extract information from video datasets. The influence of the electron beam on the reaction is discussed, and changes in behavior and kinetics are examined. Sequential thresholding and image differencing are used to track propagation events and compare low electron dose rate events with high dose rate events. Radial integration of diffraction patterns is used to track crystallographic changes during degradation and identify reaction byproducts. This chapter highlights the usefulness of automated image analysis in extracting critical information from the rich video datasets

often provided by *in situ* experiments. This work was published in the journal Ultramicroscopy in 2020 and the chapter was adapted directly from that publication under personal use for this dissertation [12].

In Chapter 6 I present a summary of the collective findings of this work and discuss the power of these automated analysis toolsets for investigating not only the specific materials problems in this work, but also those in other systems. The key is the combination of EBSD microstructural characterization with automated image processing capable of capturing whatever damage is of interest. As long as the damage parameter can be captured and converted to a binary map (to mask microstructural maps from EBSD), this toolset can be applied to any materials system. Considerations for future work in the AA5083 system are discussed at both the mesoscale and nanoscale, and further refinements of the analysis toolset are outlined to improve investigations of P-S-P relationships.

CHAPTER 2. BACKGROUND AND LITERATURE REVIEW

2.1 Corrosion and the Impact of Microstructure

Corrosion generally refers to the degradation of a metal or alloy caused by a chemical reaction between the material and its environment. Most metallic corrosion reactions involve the transfer of electrons in an aqueous electrolyte, consisting of an anodic and cathodic reaction [13]. The anodic reaction often leads to dissolution and eventual catastrophic failure of the material, so it is generally used to define the severity of the corrosion. There are several different forms of corrosion, and this section discusses a select few of them that are most relevant to aluminum and its alloys, since the Al-Mg alloy system is the primary material focus in this work. The following subsections will discuss galvanic corrosion, intergranular corrosion, pitting corrosion, and the impact of different microstructural features on these types of corrosion.

2.1.1 Galvanic Corrosion

Galvanic corrosion occurs when two dissimilar metals are electrically connected while both are exposed to an electrolyte solution (enabling ionic conductivity) [13]. Different metals have different levels of activity or nobility, and this difference between two metals in contact acts as a driving force for corrosion. The Galvanic Series (Fig. 1) gives the relative nobility of many important metals and alloys [14].

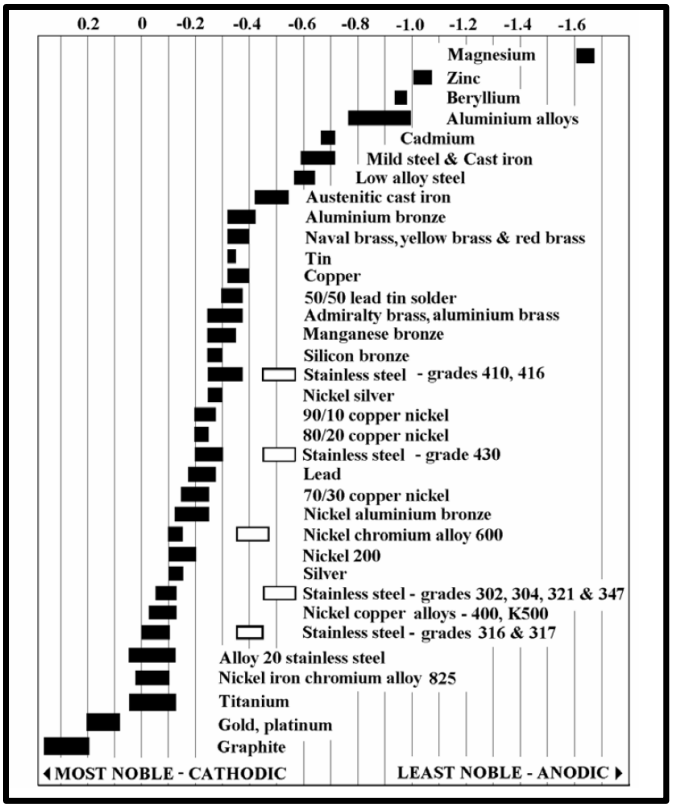

Figure 1: Galvanic series from [13] showing the relative nobilities of various metals and alloys. The more noble partner in a galvanic couple will generally be protected, while the less noble (more active) partner will be preferentially corroded.

In the diagram above, materials to the left are electrochemically more noble (less active), with the most extreme cases being graphite and gold. Materials to the right are electrochemically less noble (more active), with more extreme cases including magnesium and zinc. During galvanic corrosion, the more noble metal will act as the cathode and induce corrosion in the less noble anode (their galvanic potential difference drives corrosion). This idea is leveraged for a beneficial purpose in the application of sacrificial anodes: the metal to be protected is paired with a galvanic partner that is more active, causing the active partner to be preferentially corroded and protecting the noble metal. Figure 2 below is a schematic of galvanic corrosion that illustrates this concept.

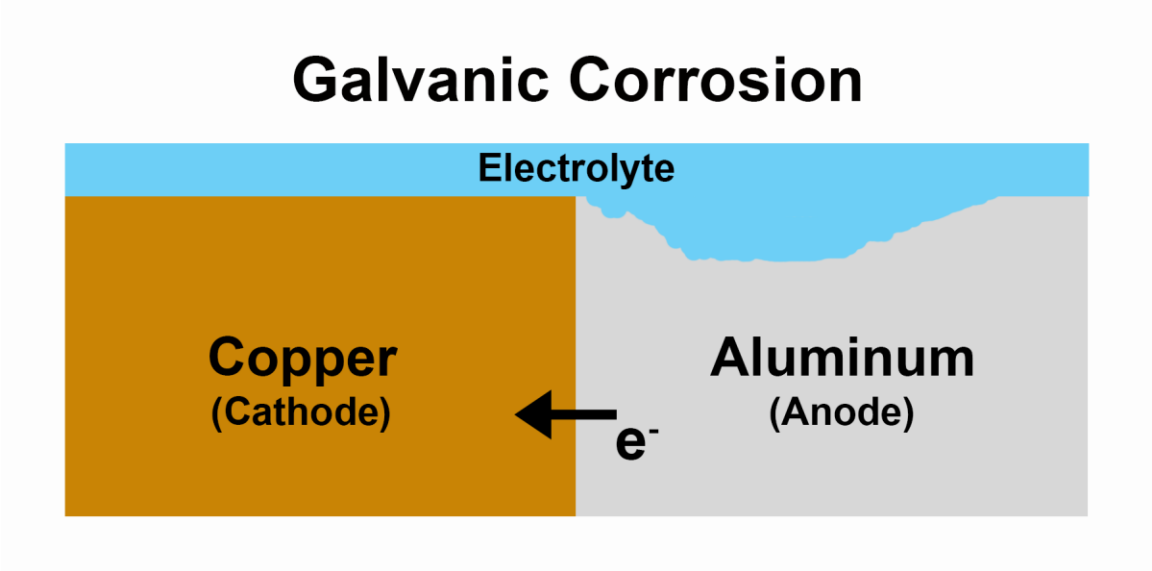

Figure 2: Schematic illustrating galvanic corrosion. The more noble metal (copper) acts as the cathode while the less noble metal (aluminum) acts as the anode and is preferentially corroded.

Copper is more noble than aluminum, so in this case the copper is protected while the aluminum is preferentially corroded. The schematic also illustrates the three necessary conditions for galvanic corrosion: 1) dissimilar metals, 2) electrical contact between the metals (enabling electron flow) and 3) exposure to electrolyte (enabling ion flow).

Typical factors that influence galvanic corrosion include: the potential difference between the two metals, the cathode-to-anode area ratio, and the distance between the anode and cathode [13, 15, 16]. The driving force for galvanic corrosion is greater for metals with a larger difference in corrosion potential, i.e. are further apart in the galvanic series [13, 16]. When it is unavoidable for a system to contain two metals that are far apart in the galvanic series, barrier coatings have been used to prevent electrical contact between the two metals (this prevents galvanic corrosion). Another factor that determines galvanic corrosion is the ratio of exposed areas for the cathode and anode: a larger cathode-to-anode

ratio creates a stronger driving force for galvanic corrosion [15]. This can be a pitfall for barrier coatings. If a barrier coating is applied to the anodic metal surface and some small local damage to the coating occurs, this exposes a small anodic surface and creates a large galvanic driving force. Mansfeld and Kenkel calculated the relationship between the anodic dissolution rate r_a and the cathode-to-anode area ratio A_c / A_A by studying aluminum alloys electrically coupled to various different alloys in an NaCl solution [15]. Equation 1 below shows that the severity of anodic dissolution is proportional to the cathode-to-anode area [15].

$$r_a = k_2 \left(1 + \frac{A_C}{A_A}\right) \quad (1)$$

The distance between the anode and the cathode also influences galvanic corrosion, as electrolyte conductivity can inhibit species transfer over long distances. This means that the contributions of galvanic influences to corrosion are limited in distance. The degree to which distance can limit galvanic corrosion is dependent on various factors influencing mass transport such as fluid velocity (whether the electrolyte is stagnant or being stirred) and the modes of mass transport taking place (migration, convection, and/or diffusion) [16].

Galvanic corrosion is crucial to understanding the corrosion behavior of Al-Mg alloys. This is because secondary phase particles in the material can form galvanic couples with the matrix, creating local anodes or cathodes that induce or inhibit localized corrosion. Preferential dissolution of active secondary phases is a primary failure mode for AA5083 specifically; this will be discussed in more detail in the next section of this chapter.

2.1.2 *Intergranular Corrosion*

Intergranular corrosion (IGC) is corrosion that follows the grain boundaries in a material, which significantly deteriorates the material's mechanical properties. This preferential attack at grain boundaries is typically due to various microstructural factors such as precipitation of active particles or depletion of passivating elements [13]. The latter is the case for the most well-known case of IGC: austenitic stainless steel. During heat treatment, chromium carbides precipitate at the grain boundaries and form a depletion zone near the boundaries that are low in chromium. Below approximately 10% chromium, these depleted zones corrode preferentially due to the loss of the passivating chromium. This metallurgical susceptibility to IGC is often referred to as sensitization. Sensitization is also well-known in Al-Mg alloys, in which the electrochemically active Al_3Mg_2 phase precipitates at grain boundaries and is preferentially attacked. This Al_3Mg_2 phase is also known as β-phase in the Al-Mg system and its precipitation and effects on corrosion behavior will be discussed in more detail in the next section of this chapter.

2.1.3 *Pitting Corrosion*

Pitting corrosion refers to severe local corrosion that occurs due to the localized breakdown of a metal's passive film. Not every metal or alloy exhibits passive behavior, but those that do often see a significant reduction in corrosion rate due to a passivating oxide layer at the surface [13]. In Figure 3 below, theoretical plots of potential vs. current density are compared for a material that exhibits passivity and one that does not. For the material showing no passive behavior, the corrosion current density continues to increase with increasing potential. In the case displaying passive behavior, however, the current

density increases only up to a certain point. At a certain potential, the corrosion current density drastically decreases and then remains relatively unchanged with increasing potential. This region in which the current density is practically unaffected by changing potential is known as the passive regime.

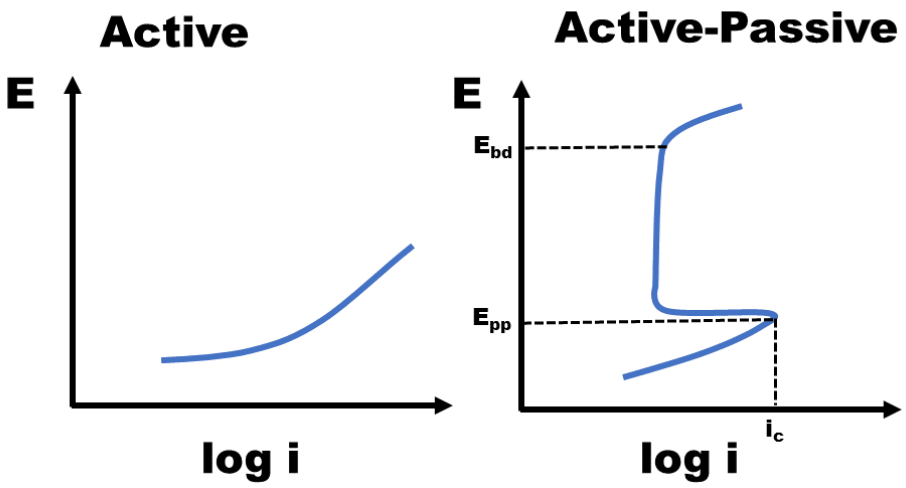

Figure 3: Schematic comparing two polarization curves for two types of material, one that shows only active behavior and one that shows active-passive behavior.

The potential at which behavior enters the passive regime is sometimes known as the passivation potential (E_{pp}) and the corresponding current density is known as the critical current density (i_c). Ideally, it is desirable for a material to have a low critical current density and low passivation potential because this makes it easier to passivate the material. The upper bound on the passive regime is known as the breakdown potential (E_{bd}) and indicates loss of stability in the passive film and an increase in corrosion activity. It is desirable for materials to have a large passive range and a high breakdown potential, as this makes it harder to drive the material out of the passive regime.

Pitting corrosion may only occur in a system that exhibits active-passive behavior: the severe local corrosion occurs due to the localized breakdown of the passive film. This breakdown is often attributed to the buildup of chlorides or other aggressive ions at the surface [17, 18]. Figure 4 below is a schematic of a theoretical cyclic polarization curve for a system exhibiting pitting behavior.

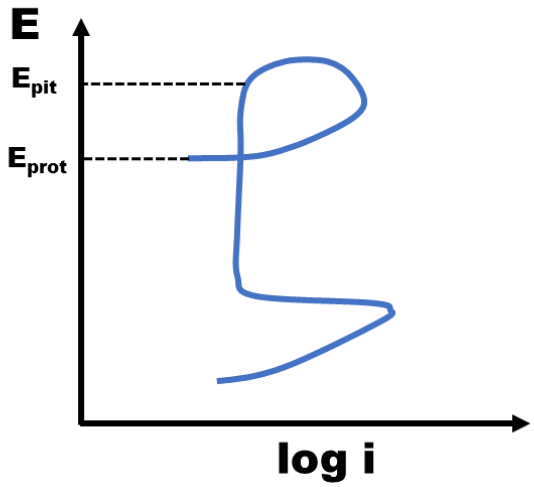

Figure 4: Schematic showing a cyclic polarization curve of a material exhibiting pitting behavior.

A loop is seen in the polarization curve above where the system exits the passive regime and enters the pitting regime, leading to an increase in current density. As the potential is lowered again, the system repassivates and the current density decreases, creating the loop. Pits initiate only above a certain potential threshold, known as the pitting potential (E_{pit}), and this pitting potential is considered an important corrosion characteristic of a metal [13]. The pitting potential is influenced by temperature, chloride concentration, inhibitors, and multiple other factors [13, 19]. Cyclic polarization experiments have shown that there is a potential below which no pitting will occur called the protection potential

(E_{prot}), or the repassivation potential (E_r) [13]. The regime between E_{pit} and E_{prot} is characterized by metastable pitting: new pits do not initiate but existing pits may grow. New breakdown of the film is repassivated, preventing stable pit initiation, but existing pits continue to grow by an autocatalytic process [13, 17]. It is desirable for E_{pit} to be at a high value and for the difference $E_{pit} - E_{prot}$ to be small, indicating that it is difficult to initiate pitting but not so difficult to repassivate the material. Pitting is not only difficult to evaluate by standard weight-loss methods, it is also insidious and is often undetected before catastrophic levels of damage have occurred. This makes pitting susceptibility an important corrosion consideration during materials design and it is therefore the experimental focus in this work.

2.1.4 *The Impact of Microstructure*

There are many factors that affect the corrosion behavior of a material, and typically the focus is on electrochemical parameters such as polarization potential, pH, temperature, inhibitors or other additives, etc. However, as demonstrated by the above sections, microstructural considerations are also important. Galvanic corrosion affects not only dissimilar macroscopic parts but also microscopic particles such as precipitates or intermetallics embedded in a matrix. Intergranular corrosion is often caused by a microstructural change that occurs due to heat treatment, as evidenced by the sensitization of austenitic stainless steels and Al-Mg alloys. Therefore, careful consideration needs to be given to the impact of microstructural features on corrosion and the way microstructure sensitive design can be leveraged to develop more corrosion-resistant materials. This final subsection discusses the role of microstructure in determining corrosion susceptibility in a more general sense, mostly for aluminum alloys, while the next section of this chapter

discusses the AA5083 alloy specifically and the literature on the role of microstructure in sensitization and corrosion of that material system.

Work in the literature investigating the influence of microstructure on the corrosion susceptibility of aluminum alloys includes studies on grain size [20-24], grain boundary character [25-29], dislocation density [20, 30], crystallographic orientation[31], and intermetallic particles [32-37]. Reports in the literature on the effect of grain size in aluminum corrosion do not show a clear dependence: Sikora et al. reported that pits were smaller and more numerous in nanocrystalline samples of Al-Mg alloys compared to coarse grained samples, while Kus et al. reported the opposite [21, 22]. Furthermore, Sikora et al. reported that the nanocrystalline samples performed worse in nitric acid mass loss testing (NAMLT) than coarse grained samples, while again Kus et al. reported the opposite (finding that the nanocrystalline samples performed better) [21, 22]. Brunner et al. found that the pitting potential decreased with increased equal-channel angular pressing (ECAP), a processing method used to produce ultra-fine-grained microstructures [20]. To the contrary, Chung et al. found that pitting potential increased with increasing passes of ECAP; although, it should be noted that the studies investigated two different aluminum alloys [23].These discrepancies raise the question of whether these differences are due to size effects or some other secondary effect caused by the processing.

While trying to consolidate experimental data to develop an equation relating grain size to corrosion (akin to the Hall-Petch equation relating grain size to strength), Ralston et al. highlighted the difficulty of isolating grain size effects from other secondary effects caused by processing such as chemical segregation, texture development, or stress buildup [24]. In truth, this is an important point about processing-structure-property relationships

in general: it is likely that the simultaneous interplay of many microstructural features determines a specific property, so developing a one-to-one relationship between a feature and a property misses potentially crucial information about other influences. However, the work by Ralston et al. did show that for materials exhibiting passivity, corrosion rate decreased with decreasing grain size according to the Equation 2 [24]:

$$i_{corr} = (A) + (B)gs^{-0.5} \quad (2)$$

The corrosion rate i_{corr} depends on the constant A which is a function of the chemical/electrolyte environment, the constant B which is a function of the material (composition or levels of impurity), and the grain size gs. It was posited that smaller grain size decreases corrosion rate in passive systems because the grain boundary density dictates the conduction rate of the oxide film [24]. For systems that did not show passivity, this equation did not hold and corrosion rate increased with decreasing grain size. This was attributed to the increased grain boundary density enhancing surface reactivity [24]. Again, it is stressed that the work by Ralston et al. attempted to consolidate corrosion data from literature and to isolate the effects of grain size as much as possible. Conflicting reports in the literature on the effect of grain size are likely due to other secondary effects that arise when the material is processed to alter its grain sizes. This highlights the importance of understanding the individual contributions as well as the synergistic interplay of multiple microstructural features when investigating overall corrosion susceptibility. In this work, grain size itself is not studied as a microstructural feature of interest in terms of pitting initiation. Instead, cold rolling is used to reduce grain size and generate different microstructures so that the other features can be investigated in a broader range of structure

space. In principal, the effects of grain sizes on pitting will likely be caused by differences in grain boundary structure (which is one of the features investigated in this study) and therefore grain size itself was not investigated.

Grain boundary characteristics have an effect on corrosion in a number of ways, particularly by influencing the precipitation of secondary phase particles (as mentioned during the discussion on IGC above). Minoda and Yoshida reported that for 6061 aluminum alloy extrusions, severe intergranular corrosion was caused by precipitate-free zones (PFZs) facilitated by random high angle boundaries [38]. Regions with a majority of boundaries less than 15° did not exhibit PFZs and therefore did not exhibit severe IGC. Shimada et al. demonstrated the use of thermomechanical treatment and twin-induced grain boundary engineering in reducing IGC in 304 stainless steel [39]. They found that slight pre-strain annealing for a prolonged time at relatively low temperatures led to a high frequency of coincident-site-lattice boundaries uniformly distributed in the sample, leading to greatly reduced IGC. Although the primary relevance of grain boundaries in Al-Mg systems is their effect on precipitation of β-phase, other aspects of grain boundaries such as misorientation angle, grain boundary plane, and conductivity or diffusivity effects can play a role as well. All of this makes grain boundaries a relevant choice of microstructural feature to investigate in terms of its influence on pitting susceptibility, and it is therefore included in this work.

Compared to other microstructural features, relatively little work has investigated the specific role of dislocation structures on the corrosion of aluminum alloys. Talianker et al investigated dislocation structures in 7XXX aluminum after different heat treatments and concluded that high dislocation density adjacent to grain boundaries was responsible

for the observed susceptibility to stress corrosion [30]. Although processing methods such as ECAP significantly change the dislocation content of the material, studies using ECAP do not often focus on this in the discussion of the altered corrosion properties, instead discussing the distribution of intermetallics or other inhomogeneities [23, 40]. However, Brunner et al. claimed that dislocation density was a controlling favor in pit morphology in high-purity Al-Mg alloys: ultra-fine-grain samples processed by ECAP exhibited highly localized pitting in depth, as opposed to the lateral crystallographic pitting of coarser-grain samples [20]. Still, further work specifically examining the effects of dislocation density on local corrosion is needed and therefore it was chosen as one of the microstructural features of interest for this work. Specifically, the local geometrically necessary dislocation (GND) density was investigated because it can be calculated directly from EBSD data.

Investigations of the effect of crystallographic orientation on pitting corrosion have indicated that there may be a dependence between planar orientation and corrosion resistance [31, 41]. Takayama et al. studied corrosion of high purity Al in different concentrations of HCl and found that the most resistant planes changed depending on the concentration [31]. At low concentrations the [42] planes showed best pitting resistance, whereas the [43] planes were most resistant at higher concentrations. Shahryari et al. showed that, for the pitting of 316 SS in an NaCl solution, both [42] and [43] planes were resistant [41]. Although work in the literature shows a dependence between corrosion susceptibility and crystallographic orientation, further work is needed in order to better understand pitting initiation in AA5083 and how it is affected by grain orientation. Therefore, grain orientation was selected as one of the microstructural features of interest for this work.

As mentioned in the discussion of galvanic corrosion, secondary phases such as intermetallic particles can have a significant effect on the corrosion behavior of a material. The formation of secondary phase particles can lead to depletion of passivating elements (as in stainless steels), cause preferential dissolution due to their active nature (as in Al-Mg alloys), or have numerous other effects. Ralston et al. studied the impact of precipitates on the pitting susceptibility of Al-Cu-Mg alloys and found that a critical size must be reached for the precipitate to have an effect [37]. It was speculated that below a certain size the precipitates could be "bridged" by the passive film, but above a certain size they would be too large and lead to instability in the oxide layer. Chen et al. studied the role of precipitate distribution in the stress corrosion of the 7050 aluminum alloy and found that samples with a distribution of fine precipitates showed better corrosion resistance that samples with coarse precipitates [44]. For the 5083 aluminum alloy, preferential dissolution of β-phase precipitates leads to severe IGC and various intermetallic particles can form microgalvanic couples and induce or inhibit pitting corrosion. This makes secondary phase particle distribution a suitable choice of microstructural feature to investigate in this work. Now that the role of various microstructural features in determining corrosion susceptibility has been discussed in general for aluminum alloys, the next section of this chapter will discuss the materials system that was the primary focus for this work: the aluminum alloy 5083.

2.2 Sensitization and Corrosion of the AA5083 Alloy

AA5083 is a medium strength, non-heat-treatable aluminum alloy that is of interest in marine applications due to its light weight and typically excellent corrosion resistance

[45, 46]. Its primary alloying element is Mg (4-4.4%), a characteristic of all 5XXX series aluminum alloys, and it is generally also contains Mn, Cr, Fe, and Si [32]. Although it generally shows good corrosion resistance, AA5083 can become susceptible to intergranular attack due to a phenomenon known as sensitization. Sensitization occurs when the alloy is exposed to moderate temperatures (50-250 °C) for an extended time and results in the precipitation of Al_3Mg_2 particles [47, 48]. When these precipitates (also known as β-phase) form at the grain boundaries, they can cause severe intergranular corrosion and lead to stress-corrosion cracking (SCC) [25, 49-51]. By better understanding the influence of different microstructural features (including secondary phase distribution) on the corrosion resistance of AA5083, microstructure sensitive design can be used to help prevent such catastrophic failure.

Of all the possible microstructural features that could influence the corrosion of AA5083, the most well-documented and supported is the presence of β-phase precipitates [32, 45, 47, 48]. The β-phase is electrochemically active compared to the matrix, so it dissolves preferentially and destroys the integrity of the grain boundaries [32, 49]. Therefore, it is expected that increased coverage of grain boundaries by the β-phase would result in more severe intergranular corrosion. Searles et al. confirmed this by showing that the ductility of AA5083 tensile samples in a corrosive solution was directly related to sensitization time, as shown in Figure 5 below [45].

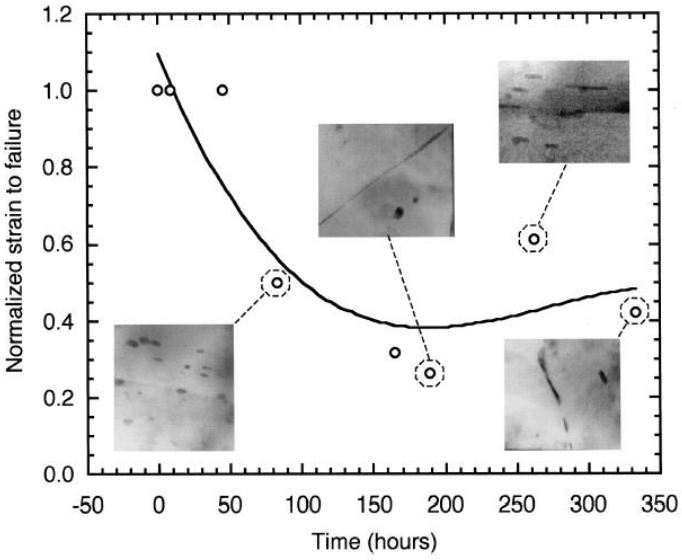

Figure 5: Normalized strain to failure vs sensitization time, with insets showing TEM micrographs of β-phase precipitation, from [40].

With increasing sensitization time, the fractional coverage of grain boundaries increased until a continuous β-phase film was formed; continuous coverage corresponded to the lowest ductility in the samples due to the severe corrosion of the grain boundaries. Some ductility was recovered for samples sensitized for even longer times, because the continuous β-phase film eventually broke down into discrete particles again. Furthermore, it was shown that β-phase exhibits a passive region between -1.4 V and -0.9 V and when samples were polarized within this range, practically all ductility was restored [45]. Even samples that had a continuous β-phase coverage at the grain boundaries saw a full recovery of ductility when polarized within the passive region for β-phase because there was no selective dissolution at the grain boundaries. Other work, by Tan and Allen, studied the effect of thermomechanical treatment on sensitization and corrosion [32]. Treated samples performed better in mass-loss corrosion testing, which was attributed to a combination of diminished texture, equiaxed grains, and altered precipitates [32]. It was found that the

untreated samples had a strong [42] texture that favored rapid and continuous coverage of the β-phase, whereas the treated samples showed no distinct texture and grain boundary coverage by β-phase was less continuous. Gao and Quesnel studied stress corrosion cracking characteristics in sensitized AA5083 and showed that incubation time and initial crack growth rate depend strongly on the amount of β-phase precipitates, as seen in Figure 6 [49].

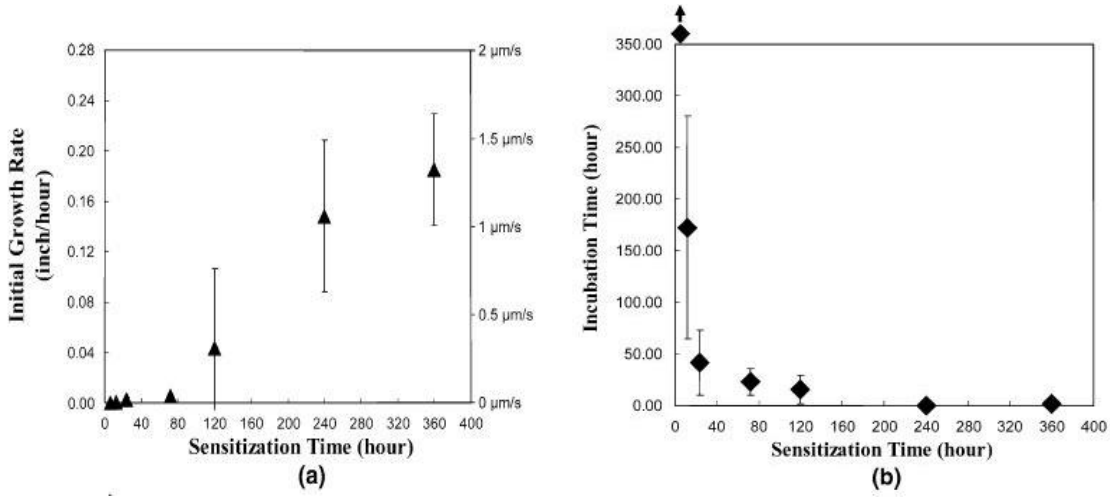

Figure 6: Initial stress corrosion cracking growth rate and incubation time as a function of sensitization time for AA5083, from [44].

Clearly, precipitation of β-phase at grain boundaries has a significant detrimental effect on the intergranular corrosion resistance of AA5083, so there has been much interest in what factors affect this precipitation. The literature on the effect of grain boundary character shows conflicting reports in regard to the effect it has on sensitization of AA5083. Davenport et al. reported that low-angle (<20°) boundaries did not show β-phase precipitation, while Kaigorodova et al. reported observing β-phase at boundaries with misorientation angles of 5-10° [25, 27]. Scotto D'Antuono et al. reported that β-phase was more prevalent at low misorientation angles than high angles, but that the size of the

precipitates was much smaller at low angles [26]. However, Yan et al. claimed the opposite in that more precipitates formed at higher angle grain boundaries [29]. Yan et al also suggested the importance of grain boundary plane in combination with misorientation angle, reporting that boundaries with plane orientations near to [43] may have greater resistance to β-phase precipitation [29]. These investigations show that more work is needed to better understand the role of grain boundary character in the corrosion susceptibility of AA5083.

Work in the literature investigating the role of other secondary phase particles, in addition to β-phase, on the corrosion of aluminum alloys is abundant [3, 20-24p]. Tan and Allen, as well as Ferreira et al., characterized the surface potentials of the common intermetallics in AA5083, giving their relative nobilities compared to the matrix (shown in Figure 7 below) [32, 33].

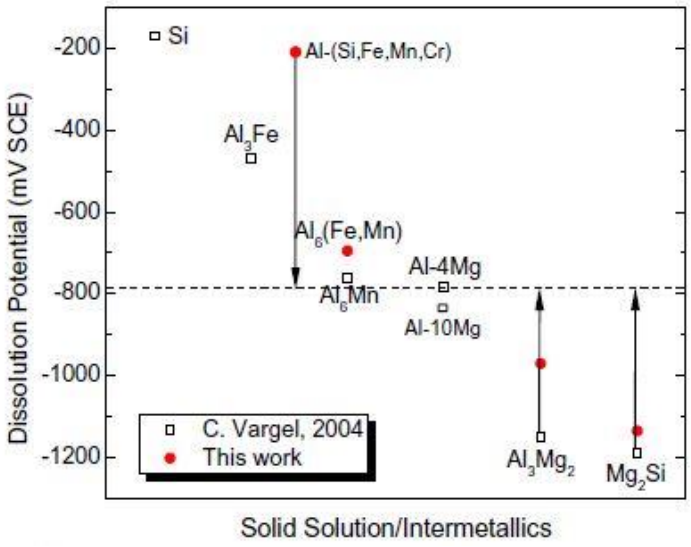

Figure 7: Comparison of the surface potentials of several precipitates as measured in [30] using SKPFM. The dotted line indicates the potential of the matrix. More noble potentials are above the dotted line while more active potentials are below it.

In the AA5083 system, intermetallics generally fall into two categories: Fe-rich and Mg- rich. Fe-rich phases such as Al-(Si,Fe,Mn,Cr) and Al_6(Fe,Mn) are relatively noble compared to the matrix and so promote pitting and localized corrosion in the adjacent matrix. Mg-rich phases such as Al_3Mg_2 (β-phase) and Mg_2Si are more active than the matrix and experience preferential dissolution. Ferreira reported that presence of Si or Cr is not as important in Fe-rich phases, as Al-(Si,Fe,Mn,Cr) and Al_6(Fe,Mn) showed similar corrosion behavior [33]. These intermetallic particles can galvanically induce or inhibit pitting the sample matrix, but work in the literature also suggests they influence β-phase precipitation [52-54]. Goswami et al. studied β-phase precipitation of sample sensitized at 100 °C for various times and found that samples sensitized for less than 45 days showed no β-phase at dislocations or dispersoids, but solely at grain boundaries[53]. However, after 45 days samples showed small amounts of β-phase precipitation at intragranular dispersoids. Yan and Hodge found that β-phase formed directly on Al6Mn dispersoids and near Al_6(Mn,Fe) dispersoids, with dislocation bands connected the β-phase to the Al_6(Mn,Fe)[54]. Such dislocation bands are thought to facilitate β-phase precipitation through pipe diffusion. The precipitation of β-phase particles, as with many other materials phenomena, depends on the interplay of multiple microstructural features including dislocation structures, secondary phase particles, and grain boundary character. This emphasizes one of the main ideas of this work: better understanding how these various microstructural features interact is critical to engineering materials with superior corrosion resistance.

2.3 Electron Microscopy Characterization

In order to understand the interplay of microstructural features and how it affects the corrosion behavior of materials, the features must be characterized in detail in the samples and the corrosion behavior must be captured. Electron microscopy enables such a detailed characterization at both the mesoscale and the nanoscale. In particular, EBSD provides rapid characterization of relatively large areas and is the primary characterization tool in this work. EBSD characterization is augmented by chemical analysis and electron microscopy imaging to fully capture both the sample microstructure and the corrosion behavior so that statistical analysis can be used to generate correlations between local microstructure and pitting initiation. For nanoscale analysis, developments in experimental methodologies were utilized to capture real-time dynamic corrosion behavior through *in situ* electron microscopy. The following subsections discuss the operating principles of these electron microscopy tools first at the mesoscale then at the nanoscale.

2.3.1 Mesoscale Characterization

Electron microscopy is a powerful tool for rapid microstructure characterization at the mesoscale. Scanning electron microscopy (SEM) uses a rastered beam of electrons that scans back and forth across the sample surface generating a variety of signals that can be used for characterization (Fig. 8). The schematic below illustrates the interaction volume between the incident electron beam and the sample, as well as listing a select few of the many signals produced by that interaction. The signals most relevant to this work include secondary electrons (SEs), backscattered electrons (BSEs), and x-rays.

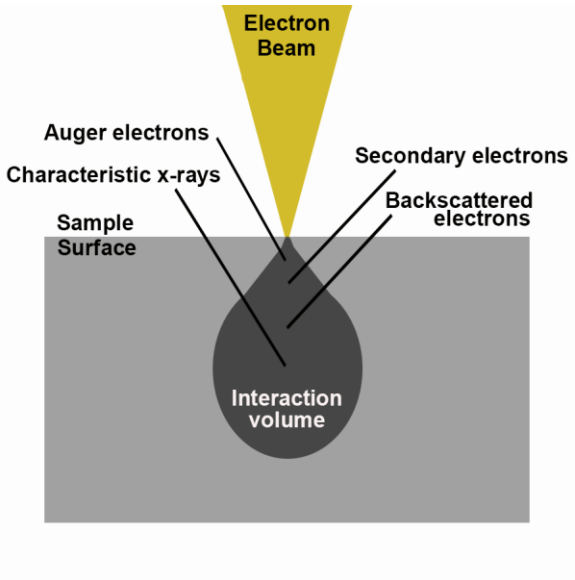

Figure 8: Schematic illustrating the interaction between electron beam and sample during SEM, as well as some of the signals generated by that interaction.

SEM is often used to examine aspects of the sample surface such as the quality of surface finish, the presence of contamination or scratches, the distribution of various secondary phase particles, fracture morphology, etc. Secondary electrons are ejected from the sample by inelastic collisions between the electron beam and the atoms of the sample. They are emitted from the region of the interaction volume at or near the sample surface, making SE imaging quite useful for examining sample topography and surface features such as corrosion pits.

Backscattered electrons (called so because they originate in the incident electron beam and are scattered back from the sample) are emitted at depths further into the interaction volume and are the result of elastic collisions between the incident electrons and the atoms of the sample (rather than inelastic). BSEs are less sensitive to surface topography because they are emitted from deeper in the sample. However, since heavier atoms scatter more electrons, BSE signal is proportional to the atomic number (Z) of the

sample atoms and therefore is sensitive to chemical composition (unlike SE). This makes BSE imaging useful for investigating the presence of different chemical phases, such as intermetallic particles whose composition is largely different from that of the sample matrix. However, such Z-contrast imaging relies on a large difference in atomic number for various constituents of the sample. If Z is too similar for the different phases, the contrast will not be very clear. Furthermore, BSE imaging does not give the chemical composition of the phases but can merely show contrast between them. BSE imaging alone would not be a suitable method for chemical analysis of the sample surface.

Energy dispersive x-ray spectroscopy (EDS), on the other hand, is used for precisely that. Another one of the useful signals generated when the electron beam interacts with the sample is known as characteristic x-rays. The process by which these x-rays are generated is as follows. During interaction with the electron beam, a core atom of the sample is ejected. A higher energy electron will relax and fill the hole left behind by the ejected atom. Figure 9 below shows a schematic of such an event.

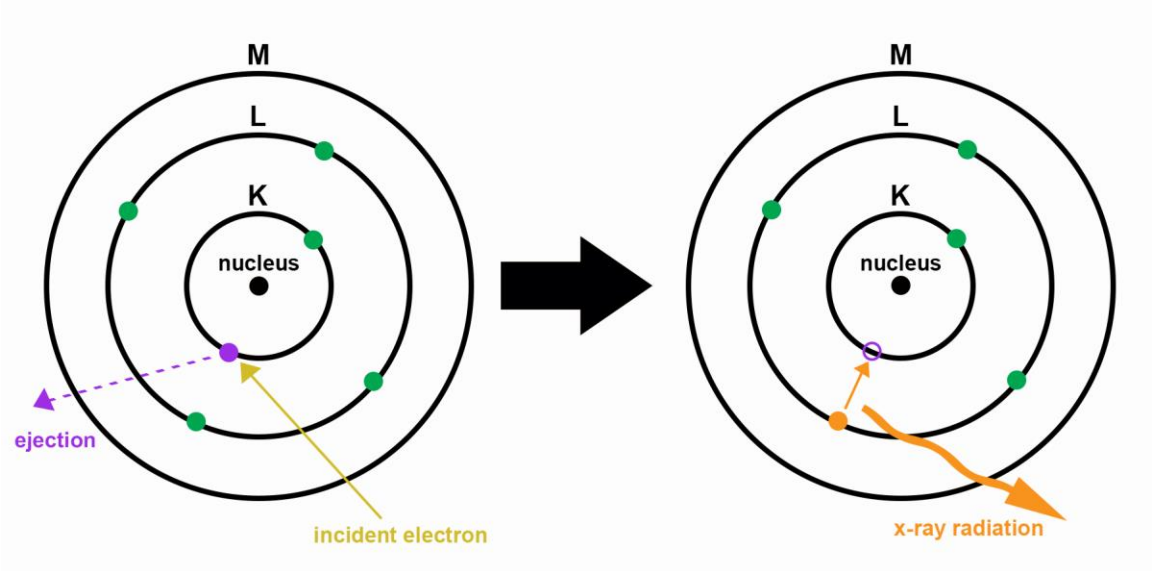

Figure 9: Schematic illustrating the ejection of a core electron and the relaxation of a higher-level electron that results in the emission of a characteristic x-ray.

Due to the atom changing energy states, an electromagnetic wave is released that has energy equal to the energy difference between the two states. The energy levels of different atomic shells are quantized and known, so the energy of this x-ray is characteristic to the atom from which it is emitted (hence the name characteristic x-rays). Therefore, these x-rays can be used as fingerprints to identify the chemical composition of a sample. The x-ray signal is described by the energy level the electron was ejected from and the number of energy levels the relaxation event occurred across. A common signal in EDS analysis is the Kα emission. This means that the electron was ejected from the K shell (pictured in Figure 9 above) and the relaxing electron came from one shell higher. If the relaxing electron came from two shells away, it would be a Kβ emission. In the SEM, the electron beam is rastered across the sample which means EDS analysis can be done at a single point, in a line, or in a two-dimensional map, enabling detailed chemical analysis of relatively large areas. Auger electron spectroscopy (AES) is a similar chemical analysis

technique in which electrons are the analysed signal rather than x-rays. However, the interaction depth is only a few nanometers for AES (opposed to a few microns for SEM/EDS) and is more suited to analysing lighter elements and it is not utilized in this work.

The final mesoscale characterization tool to be discussed in this subsection is electron backscatter diffraction (EBSD). As the incident electron beam interacts with the sample, electrons are scattered in many directions from within the interaction volume. Some of these electrons satisfy the Bragg condition and are coherently diffracted from the lattice planes of the sample. These diffracted electrons form two cones (from the top and bottom of the lattice plane) that are characteristic to the family of planes from which they are diffracted. As the cones of electrons exit the surface, they intersect the phosphor screen of the EBSD detector and form what are known as Kikuchi bands (Fig. 10) [7]. These Kikuchi bands form the characteristic diffraction pattern that EBSD analysis is known for. Each point in the rastered scan gives a pattern that can be used to determine the crystallographic orientation of that point (the orientation of the lattice planes with respect to a reference coordinate system).

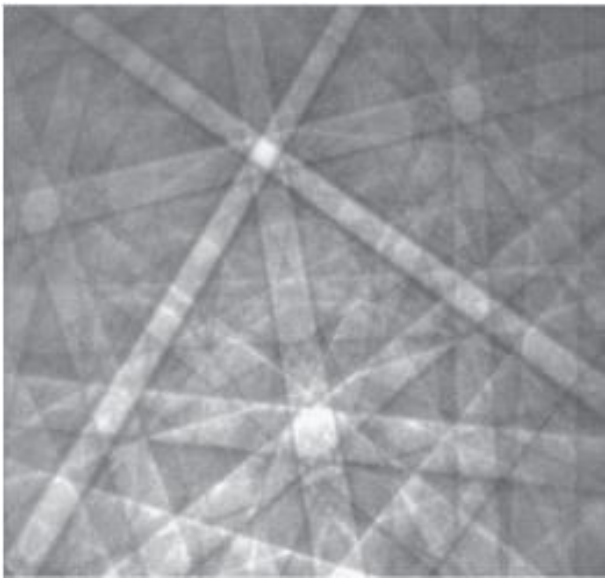

Figure 10: EBSD pattern formed by Kikuchi bands in single-crystal silicon, from [7].

With the development of EBSD analysis software, indexing the patterns using the Kikuchi bands is now an automated process that requires little work on the part of the user. The critical information is the position and angle of the bands that form the EBSD pattern. The most common method for determining this information involves the Hough transform. This is an image-processing approach that has been modified to detect bands in an EBSD pattern by transforming each band into a peak (based on its position and angle), reducing the problem from band-finding to peak-finding. A Hough transform for Kikuchi band analysis is shown in Figure 11 below.

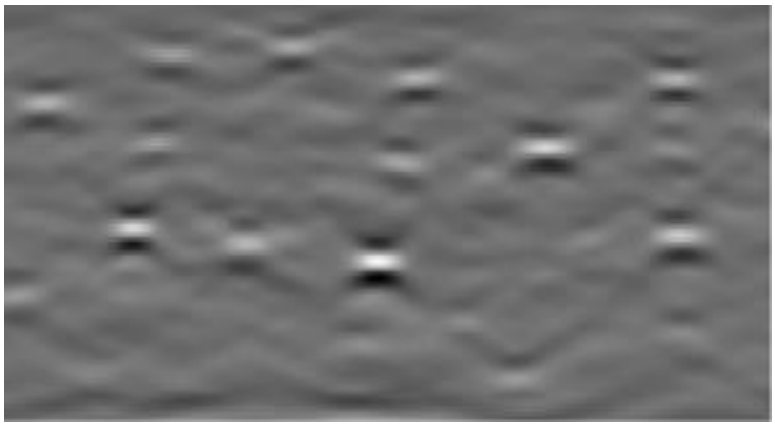

Figure 11: Hough transform of an EBSD pattern from titanium, from [7].

By tracking the peaks and comparing to calculated lattice arrangements, the patterns are indexed and the orientation is given for every point. This is the primary goal of EBSD. From this crystallographic orientation information, one may create the object most commonly associated with EBSD: the inverse pole figure (IPF) map. An example is shown below in Figure 12.

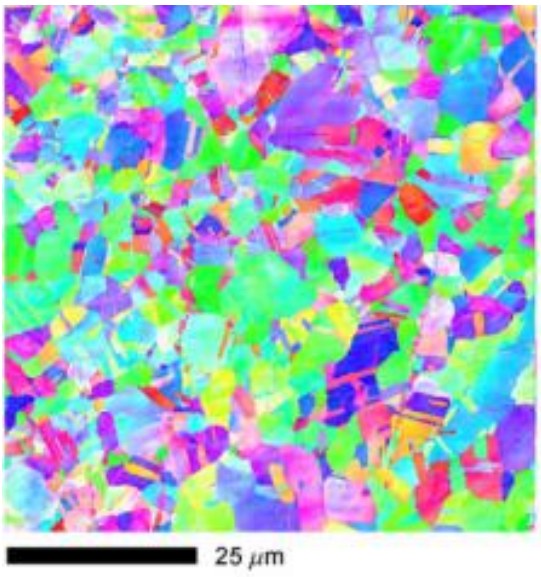

Figure 12: IPF map for a nickel sample, from [7]. Each point is color-coded corresponding to its orientation (crystal direction aligned with the sample normal) varying continuously between [001], [111], and [110].

Each point in the scanned region is color-coded based on its orientation with respect to the reference coordinate. Visually, one can see grains as the different colored objects in the map. However, EBSD orientation data provides much more than a grain map; several other important characteristics can be derived from this information. Grain size and texture analysis, grain boundary analysis, and phase identification are all commonly used applications of EBSD. This makes EBSD a powerful characterization tool, since it provides such a wealth of information over a relatively large area in relatively short amount of time. These attributes of EBSD make it ideal for use in a statistical microstructural analysis.

Grain size and texture analysis are two of the most common applications of EBSD and are conceptually straightforward when one looks at the IPF map. The orientation of every indexed point is known with respect to a reference frame (color-coded in the IPF map) and can be plotted in an IPF to show if there are higher concentrations of certain orientations. This is usually plotted as multiples of a random orientation, as shown in Figure 13 below.

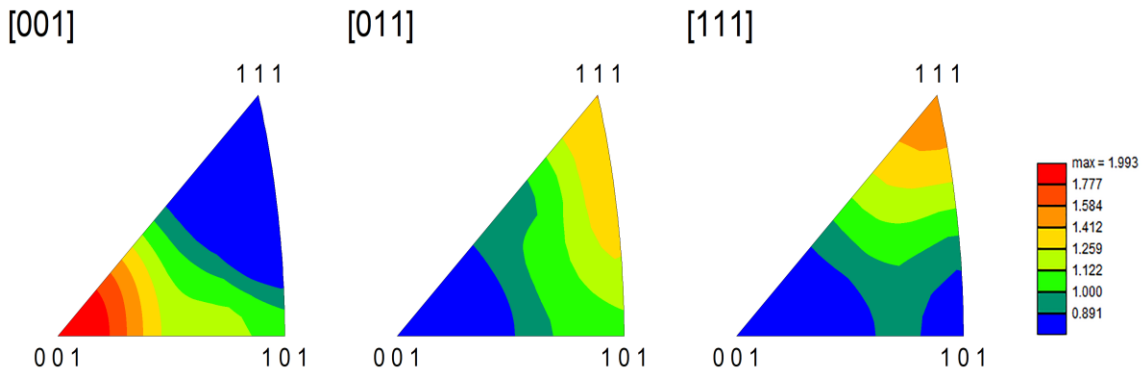

Figure 13: Example texture analysis for an AA5083 sample. The different IPFs show different reference sample directions. The colorbar shows the frequency of the orientation compared to a random distribution (e.g. 1.5 times more frequent than in a random distribution).

Each IPF shows the distribution of orientations with respect to a different reference sample direction. By plotting how frequent certain orientations are compared to a random distribution, one can determine if there is a strong preferred texture in the sample. Values that are close to one show a random texture, but if there were values such as five times random then that would indicate a strong texture in the corresponding orientation.

Grain size measurements are also straightforward (rough estimates can even be made visually based on the IPF map) since grains are identified in the scan based on the indexed orientations in different regions. Labelling grain boundaries is straightforward in much the same way. By identifying different grains based on changes in orientation, and transitions between orientations seen in the EBSD patterns, grain boundary maps are generated. The misorientation between grains can be calculated so that grains can be classified into different types such as low-angle boundaries, coincident site lattices, and random high-angle boundaries. Additionally, in samples that have multiple phases present (such as face-centered cubic and body-centered cubic), these phases can often be

distinguished by their EBSD patterns and are indexed accordingly. This allows phase maps to be constructed from EBSD analysis in addition to grain maps. This work does not require the phase mapping capabilities of EBSD but does utilize texture analysis of the pits and grain boundary mapping.

Another important piece of information that can be derived from EBSD analysis is the local geometrically necessary dislocation (GND) density. GNDs are a type of dislocation caused by geometrical constraints of the crystal lattice and are stored in strain field gradients. These long-range distortion gradients are related to heterogeneous deformation. The theory of GNDs was introduced by Nye, who described a tensor to calculate the dislocation density. This was adapted by Kroner to calculate the dislocation density in terms of elastic distortion using curvature (Equation 3) [8].

$$\alpha_{ik} = \kappa_{ki} - \delta_{ki}\kappa_{mm} - \epsilon_{klj}\frac{\partial \varepsilon_{ij}^{el}}{\partial x_l} \tag{3}$$

The dislocation density tensor α is related to the curvature κ of the orientation field and the elastic strain ε^{el}. Assuming negligible elastic strain, the dislocation density can be calculated from the curvature of the crystal lattice:

$$\alpha_{ik} = \kappa_{ki} - \delta_{ki}\kappa_{mm} \tag{4}$$

Equation 4 above shows that that dislocation density tensor can be calculated from the curvature of the crystal lattice. From EBSD, the curl of the orientation field can be used to calculate the L1 norm of Nye's tensor and give an approximation of the GND density [9].

2.3.2 Nanoscale Characterization

Traditionally, corrosion studies are macroscopic and/or *post mortem*. Macroscopic studies can miss important localized information, such as in the case of pitting. Weight-loss studies are poor measures for pitting corrosion because the global corrosion rate may be low while critical areas have been completely perforated by pits, leading to failure. Studies that are done *post mortem* give little information on kinetics and sometimes no direct information on mechanisms. Many corrosion studies address one of these issues or the other but fail to address both. However, with the advancement of transmission electron microscopy (TEM) sample holders and electron detection technology, investigations of many dynamic processes can now take place inside an electron microscope. TEM provides high spatial-resolution characterization of materials at the nanoscale that goes beyond imaging, including chemical and structural analysis. In this work, TEM imaging was used to track the evolution of dynamic corrosion events in real-time. Observations of the propagation behavior and kinetics were made and automated image analysis was used to quantify the behavior. Diffraction analysis was also used to study the evolution of the polycrystalline diffraction pattern during degradation and to identify byproducts of the reaction.

In contrast to SEM, the operating principle of TEM is to transmit a high-energy (typically 200 to 300 kV) electron beam through a sample that is only a few hundred nanometers or less thick (thin enough for the beam to pass through) [55]. The interaction between the sample and the electron beam does, however, generate similar signals to those in SEM. X-rays and scattered or diffracted electrons can be used to analyze the chemical or structural nature of the sample (such as in EDS) and to image it.

In TEM imaging, there are several modes of contrast. Mass-thickness contrast is a result of Rutherford scattering of electrons. Rutherford scattering is a strong function of the atomic number Z and the thickness, meaning thicker or higher-Z areas will scatter more electrons off axis than thinner or lower-Z areas. This causes thinner areas to appear lighter and thicker areas to appear darker in bright-field imaging (collecting the direct transmitted beam). This is one of the most commonly-seen forms of contrast in TEM imaging. Another mode of contrast is diffraction contrast, in which Bragg diffraction dictates the brightness in the image. Different regions of a crystalline sample will diffract the incident electrons differently based on their lattice planes, and this can be utilized to form images in which bright areas satisfy the Bragg condition and dark areas do not. This is less useful in polycrystalline samples with small grain size because for any illuminated area there will be many different grains contributing to the diffraction. Finally, phase contrast results from the relative phase shift of the electrons in the beam as they are transmitted through the sample and is primarily used in high-resolution imaging of crystal lattices. The primary contrast mode utilized in this work is mass-thickness contrast, seen as the film undergoes oxidation and eventual dissolution. In addition to real-space imaging, diffraction-space imaging was used to track the crystallographic evolution throughout the experiments.

The recent development of specialized liquid cell TEM holders has extended the investigation of active corrosion events to aqueous environments within an electron microscope [10, 56-60]. These liquid cell holders typically work by encapsulating the liquid layer in between two silicon chips, each of which has an electron-transparent silicon nitride membrane that acts as a viewing window [11]. The chips are hermetically sealed, often using O-rings and clamps, to isolate the liquid from the vacuum of the TEM column.

The thickness of the liquid layer can be adjusted using spacers, and the flow can be controlled using a syringe pump connected to inlet and outlet tubes throughout the chips. Some holders even have biasing capabilities which allow a potential to be applied to the sample. An example of a commercial liquid cell holder and chipset from Protochips Inc. is given in Figure 14 [61].

Figure 14: Protochips Poseidon Select liquid cell TEM holder [58].

LC-TEM presents many new possibilities for corrosion studies, but it also comes with its own challenges, including understanding the electron beam effects and quantifying the observed behavior. A number of deleterious effects arise from the interaction of the electron beam with the sample and the liquid in which it is encapsulated, including beam-induced heating, changes in solution chemistry, and the formation of radiolytic species [10, 11, 58]. These effects on the system environment are still not well understood, and any analysis of *in situ* liquid cell corrosion experiments should acknowledge these potential factors. Previous studies in the literature report that beam heating is likely not significant

for corrosion experiments, although the creation of radiolytic species may alter the system pH [58]. The beam may also affect the electrical potential of the system. Since both pH and operating potential play an important role in determining corrosion behavior, increased uncertainty in these makes analysis difficult. However, strategies are being developed to minimize beam effects and to better understand their influence on the system so that investigators can take full advantage of the many opportunities created by liquid cell electron microscopy [59].

LC-TEM provides a wealth of information about localized corrosion kinetics and mechanisms, corrosion front morphology, corrosion byproducts, and the influence of microstructure on corrosion pathway by providing direct observation of active corrosion events at nanoscale spatial resolution with high temporal resolution (over 1000 frames per second with the latest generation of electron detectors) [58, 59, 62]. This proves especially useful for diffraction studies, in which the changes in diffraction signal may occur quite rapidly or subtly. *In situ* TEM corrosion experiments provide a unique opportunity to gain insight about local corrosion mechanisms that can enhance our understanding of the influence of microstructure on corrosion.

CHAPTER 3. EXPERIMENTAL METHODS

The experiments performed in this work fall into two main project areas (at two different length scales): 1) correlating pitting initiation to local microstructure using a combination of electron microscopy characterization and automated image analysis (at the mesoscale) and 2) extracting information on dynamic corrosion events and how they are influenced by electron dose rate using *in situ* TEM methods and image processing routines (at the nanoscale). This chapter presents the objectives of the work and then goes into the experimental details for the various techniques and design parameters used for the investigations.

3.1 Mesoscale Analysis Framework and Corrosion Testing

For this study, AA5083-H116 samples were processed with three different thermomechanical treatments to create a range of microstructures to be investigated: 1) as-received, 2) 50% cold rolled and annealed, and 3) 70% cold rolled and annealed. Sheets of AA5083-H116 were obtained from a commercial source with the nominal composition given below in Table 1.

Table 1: Nominal composition of AA5083 sheet from commercial source.

Element	Aluminum	Magnesium	Silicon	Manganese	Chromium	Iron
Wt%	92.9-94.1	4.0-4.4	0.4	0.4-1.0	0.05-0.25	0.4

The sheets were cut into 0.5" x 0.5" squares before undergoing cold rolling. Cold rolled samples were annealed at 400 °C for 3h and then water quenched to ensure undesired Al_3Mg_2 precipitation did not occur. After cold rolling and annealing, two batches of samples were made. One batch was left unsensitized while the other batch was sensitized at 175 °C for 72 hours. This created a text matrix of six different sample conditions, shown below in Table 2.

Table 2: Text matrix showing the six different combinations of sample condition.

Condition	As-received	50% CR + anneal	70% CR + anneal
Sensitized	x	x	x
Unsensitized	x	x	x

Samples were mechanically polished using silicon carbide papers and diamond/silica suspensions, followed by flat ion milling, to achieve a surface quality suitable for indexing in EBSD analysis. After characterization, samples were immersed in

a 3.5 wt% NaCl solution for 24 hours with no applied voltage. This condition was chosen to allow pit initiation without significant pit growth, since the goal was to investigate the early stages of pit initiation and the influence of local microstructure.

Microstructural characterization was performed using a combination of SEM imaging (both in SE and BSE imaging modes), EBSD mapping, and EDS chemical analysis. Fiducial markers were used to mark off areas roughly 250 μm x 250 μm to ensure that the same areas could be analyzed both before and after corrosion. The size of the regions was chosen to be small enough to facilitate detailed imaging of the pitting behavior but large enough to encompass a reasonable number of grains for statistical analysis. Prior to corrosion, SE and BSE imaging was used to capture the details of the sample surface. SE imaging is sensitive to surface morphology and was used to check the surface condition of the sample prior to exposure to the NaCl solution. BSE imaging is more sensitive to difference in chemical composition, which made it useful for distinguishing between secondary phase particles and the sample matrix. EDS chemical analysis was used to identify the various types of intermetallic particles and classify them as either electrochemically active or electrochemically noble compared to the sample matrix based on composition. However, BSE imaging alone was able to differentiate between the different classes of intermetallic particle (active or noble) and the matrix. This is because the Fe-rich noble intermetallics appear brighter in BSE imaging, and the Mg-rich active intermetallics appear darker. Accordingly, BSE analysis alone could be used to generate maps of the distribution of intermetallic particles on the surface, making the process quicker and more straightforward than using EDS analysis at every location.

EBSD provides rapid characterization of relatively large areas, providing microstructural details on crystallographic orientation, grain boundary character, and local GND density. The local GND density was calculated directly from EBSD scan data using the curl of the distortion field to calculate local curvature. This was used to calculate the L1 norm of Nye's dislocation density tensor, as discussed in Chapter 2.

3.2 LC-TEM

In this work, a model system of pure Fe corroded was investigated in a water vapor environment. This system was chosen to establish experimental and analytical methodologies before moving to the more complicated Al-Mg alloy system. Fe thin films, with thickness ~100 nm, were deposited directly onto the Si_3N_4 membrane in the bottom microchip of a liquid cell chipset using RF magnetron sputtering. A 99.99% purity Fe target (Kurt J. Lesker Co., Pittsburgh, Pennsylvania) was used as the source and sputtering was performed at a power of 75 watts and a pressure of 5 mTorr for 30 minutes. The microstructure of the as-deposited thin films was characterized prior to exposure to any aqueous medium using bright-field (BF) and centered dark-field (CDF) TEM imaging, annular dark field scanning (S)TEM, and electron energy loss spectroscopy (EELS) analysis in a FEI Titan operated at 300 kV. The deposited film was observed to be stable under the electron beam under vacuum conditions.

In situ observations of the oxidation process were made using a commercial liquid cell, with a chipset configured for a 500 nm liquid gap. (Protochips Inc., Morrisville, North Carolina). Prior to loading into the TEM to conduct experiments, the sample and tubing

were flushed with deionized water to check the system for leaks. Experiments were conducted without any external liquid flow, examining oxidation in a water vapor environment under ambient pressure and temperature conditions. The vapor pressure was calculated to be approximately 3.5% using the Clausius-Clapeyron equation, though it should be noted that, with these experiments, the precise environment local to the film itself is difficult to determine. The oxidation events were captured using a Gatan OneView camera (Gatan Inc., Pleasanton, California) with video recording at 100 frames per second. Videos of the oxidation behavior were collected both in real space with the TEM operating in bright-field mode and in diffraction space with selected-area diffraction patterns acquired.

CHAPTER 4. RESULTS AND DISCUSSION

4.1 Materials Agnostic Toolset

4.1.1 Motivation

Pitting corrosion is a particularly insidious form of corrosion caused by a breakdown in a metal's passive film due to a buildup of chlorides or other aggressive ions at the surface, leading to rapid localized corrosion [17, 18]. It can be difficult to detect pitting before catastrophic damage has occurred, making pitting susceptibility an important consideration in materials design. Pitting corrosion in aluminum systems has long been studied [17, 42, 63-65]. Zaid et al. investigated the impact of chloride concentration on both corrosion potential and pitting potential, finding that increased chloride content shifted both to more active values [19]. Meng et al. compared corrosion potential and corrosion current density between microcrystalline and coarse-grained aluminum and found that in the microcrystalline system pit initiation was accelerated but pit growth was impeded [66].

However, these investigations often focus on global electrochemical response of the material, looking at characteristics such as pitting potential and polarization behavior, and how this response is influenced by microstructure, but do not focus on localized behavior [17, 19, 66, 67]. Limited studies examine the influence of local microstructure on localized corrosion behavior in a statistical manner. All of the above investigations are highly important for increasing our understanding of corrosion and the various factors that influence this complex phenomenon; however, investigating pit initiation sites in terms of

local microstructure by using a large sampling and statistical analysis is an approach that has many opportunities and needs further pursuit.

The first objective of this work was to develop an analysis framework that can be used to create structure-property relations not only for corrosion investigations in Al-Mg alloys but also studies of other type of material damage (such as void formation under irradiation) in a variety of materials systems. The crux of the framework is to combine rapid microstructure characterization through EBSD with automated image analysis that quantifies the damage parameter of interest. Microstructure characterization and analysis was used to generate maps for all microstructural features of interest in each scanned region. For this work, the features of interest were grain orientation, grain boundary proximity, intermetallic particle proximity, and local GND density. Automated image processing was used to create binary pit maps from SEM images, quantifying the damage in the material. These binary pit maps were used to mask the microstructural maps so that, for every pitted pixel in the scanned region, detailed information on the microstructural features of interest was known. For example, masking the map of local GND density with the binary pit map shows the local GND density prior to corrosion for every pitted pixel. Statistical analysis is then used to examine the influence local GND density has on pit initiation. Frequency histograms show the relative pitting as a function of GND density as well as the other microstructural features of interest. The following subsections will go into detail on each step in this analysis toolset.

4.1.2 Microstructural Mapping of the Region of Interest

The two most important components for this analysis toolset are microstructural maps obtained from EBSD analysis and automated image processing of the material damage behavior. EBSD provides microstructural characterization of relatively large regions relatively quickly. For this work, the features of interest were: grain orientation, grain boundary proximity, local GND density, and intermetallic particle proximity.

The first three of these were derived directly from EBSD scan data. Intermetallic particle proximity was calculated by combining EBSD scan data with SEM imaging of the sample surface, capturing the intermetallic particles. Grain orientation analysis is the most common and well-known application of EBSD analysis. As discussed previously, the entire operating principle in EBSD is to index every point in the scan grid by identifying the Kikuchi bands captured from backscattered electrons at the detector. This gives a crystallographic orientation for each point in the region of interest, and further information such as grain size or grain boundary character can be derived from this direct measure. Figure 15 below shows an IPF map of one region of interest in a sample. A quick look at this map can give an indication of the approximate grain size in the region as well as if there is a strong crystallographic texture (for example if the grains are heavily elongated in one direction and the map is primarily in one or two colors). For this work, the important information is the grain orientation at every point in the region so that we can find the orientations of the points that become pitted.

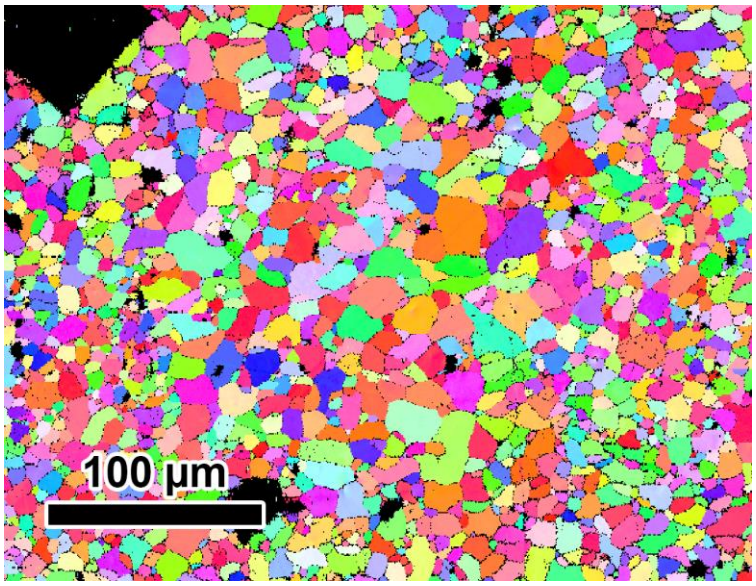

Figure 15: IPF map of one region of interest, showing grain orientation information for each point. Points with confidence index (CI) less than 10% have been blacked out.

The second microstructural feature of interest in this work is proximity of the pit to the nearest grain boundary. From EBSD analysis, having a fully indexed map of all the grains, it is straightforward to generate a map of all the grain boundary locations and their misorientation angle. For this work, however, grain boundaries were not differentiated by misorientation angle and were all treated the same (future enhancements of the analysis toolset will include differentiating between high-angle and low-angle grain boundaries). In this way, proximity heatmaps like that shown below in Figure 16 were generated for each scan. Each pixel has a value based on the distance to the nearest grain boundary: pixels close to grain boundaries are blue and pixels far away from any grain boundaries (such as in the interior of a large grain) are yellow. Again, these proximity maps were later masked with binary pit maps to give the grain boundary proximity for every pitted pixel so that correlations could be made between grain boundary location and pit initiation sites.

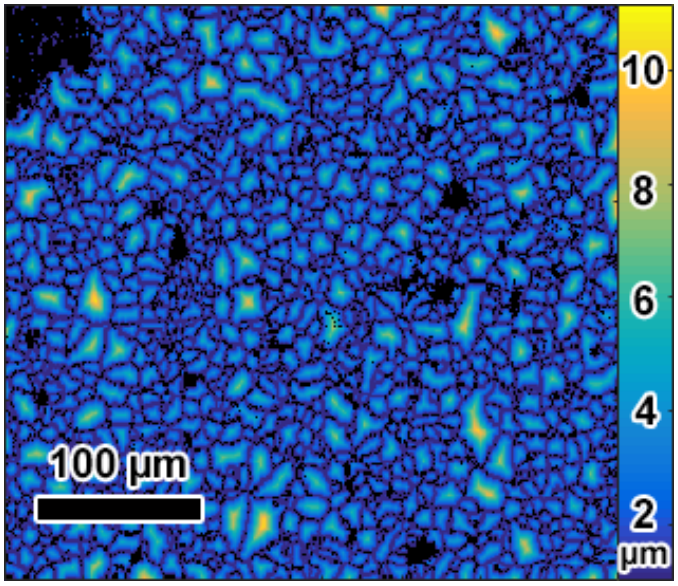

Figure 16: Grain boundary proximity map of a region of interest, showing distance to nearest grain boundary in microns. Pixels with CI < 0.1 are blacked out.

Intermetallic particle proximity maps are generated using the same type of analysis as for grain boundary proximity, except applied to binary intermetallic particle maps. These maps are generated from BSE images by a simple global thresholding: Fe-rich intermetallics that are noble to the matrix appear bright and Mg-rich intermetallics that are active to the matrix appear dark. EDS analysis was used to was used to confirm the composition of the various intermetallics in the system and categorize them as either active or noble, confirming that the noble intermetallics were bright and the active ones were dark. Figure 17 below shows an EDS line scan identifying two noble intermetallic particles, one that is rich in both Fe and Mn and one that is rich in Mg without Fe, both appearing bright relative to the matrix.

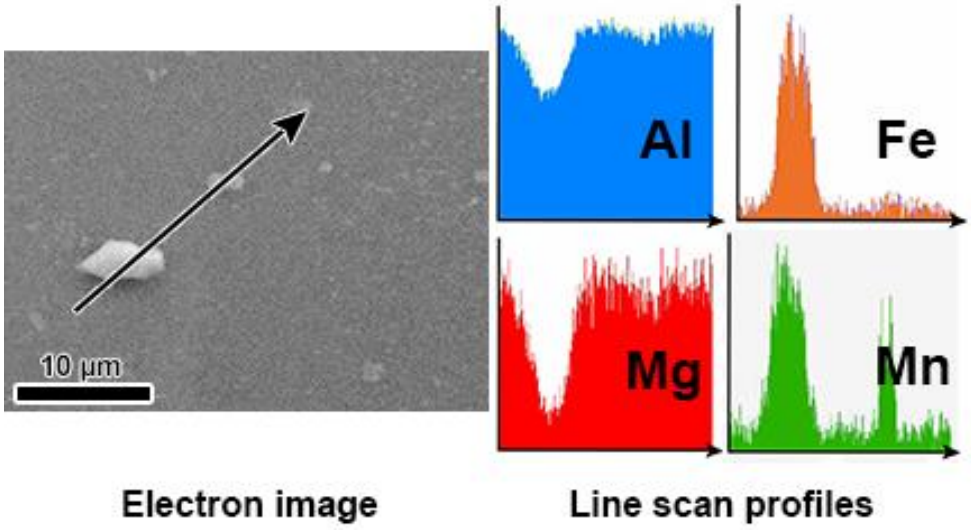

Figure 17: Electron imaging showing EDS chemical analysis line scan across two intermetallic particles, with corresponding chemical profiles.

This confirmation meant that thresholded BSE images were sufficient to make intermetallic particle maps. Figure 18 below shows a raw BSE image and the corresponding active/noble binary intermetallic particle maps. From the binarized maps, it is evident that the thresholding does an adequate job of capturing the intermetallic particles. Furthermore, you can see that the noble intermetallics are larger and more numerous than the active particles. Indeed, for some regions there were too few active particles to match with the scan data which made them unusable. For the usable regions, however, thresholding the BSE images resulted in accurate intermetallic particle maps for both active and noble particles. This simplified things greatly because BSE imaging is much quicker and more convenient than repeated EDS analysis.

Figure 18: Raw BSE image of a region of interest (left) with corresponding binarized maps of noble intermetallics (middle) and active intermetallics (right).

These binarized intermetallic particle maps were used to create proximity maps using a distance transform in MATLAB. Figure 19 below shows one such map for noble intermetallics. As before (with the grain boundary proximity maps), each pixel is assigned a value corresponding to its distance to the nearest non-zero pixel (in this case a pixel belonging to a noble intermetallic). Pixels that are below a confidence index of 10% (CI < 0.1) are blacked out and not used in the analysis. Most of these unused pixels come from the intermetallic particles themselves which are not indexed in the EBSD analysis. The colorbar has been labeled to show the distance values corresponding to the colors in the map. In this case, the maximum distance any pixel is from its nearest intermetallic particle is roughly 60 microns.

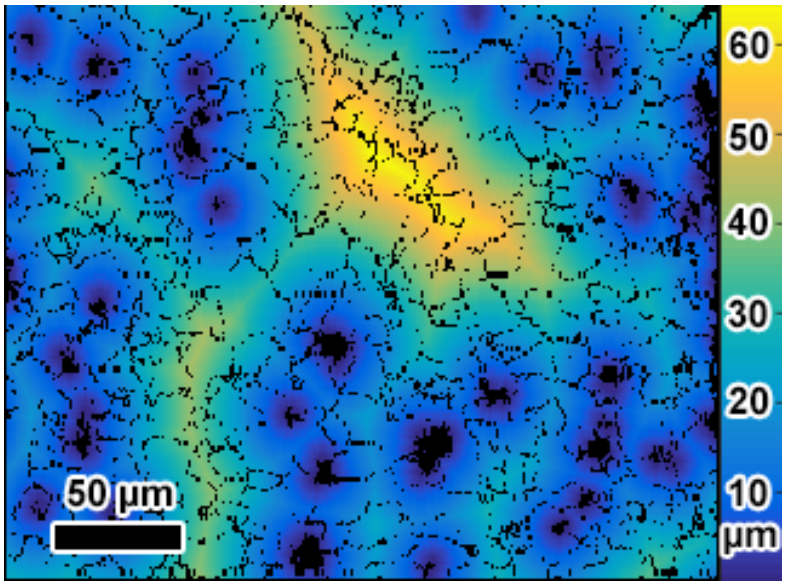

Figure 19: Noble intermetallic proximity map of a region of interest, showing distance to nearest noble intermetallic in microns. Pixels with CI < 0.1 are blacked out.

An important consideration during this analysis is the fact that these proximity calculations are made only using the information in each image individually. Nothing of the area outside the image is known. This means that there could potentially be some inaccuracies due to the boundary condition. For example, in the top center of Figure 19 above there are some pixels calculated to be 50 or 60 microns from the nearest intermetallic. Well, that is true for the intermetallics in the image but there could be an intermetallic just outside the field of view of the image. So physically those pixels would be much closer to an intermetallic, but these calculations would not indicate it. This is a potential risk for pixels near the edge of the image. In order to account for this, two steps were taken. First, a masking border was placed around the edge of each proximity map after it was calculated. The width of this border was equal to half of the maximum value in the map (half of the largest distance any pixel was to its nearest intermetallic) and is shown below in Figure 20. This spatially moves the boundaries of used data away from the edge

of the image, reducing the likelihood that an intermetallic outside the image is causing an error. The proximity map is calculated using the full image, but pixels near the edge are discarded. Second, when the relative pitting histograms are calculated, they only include pixels in the map that have a value less than the border width. This second step affects all remaining pixels that survived step one; that is to say, any pixel that had a distance value greater than the border width was discarded. This means that even if a pixel was spatially at the edge of the border, it would have to have a value less than the border width, meaning it could not be influenced by a particle outside the image. This ensures that, while the amount of data used to create the histograms is reduced, we are completely confident that these proximity values are accurate and not influenced by boundary effects.

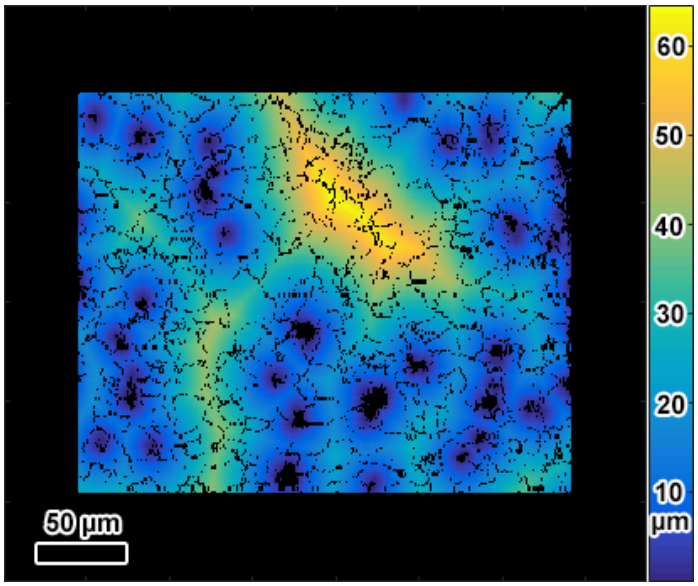

Figure 20: Schematic showing the approach used to mitigate edge effects in intermetallic particle proximity maps. A border having width equal to half of the max distance in the map is used to mask the edges of the region of interest.

For clarity, this process will be described for Figure 20 above. First, a proximity map is calculated from a full binary intermetallic particle map. The maximum value in the map is found to be roughly 90 microns. A border with a width of 45 microns is then set around the edge of the map (this border is shown in Figure 20). None of the blacked-out pixels masked by the border are used to generate the relative pitting histograms. The histograms are calculated from the remaining map inside the border, except for those pixels with a value greater than 45 microns. This is because pixels with values greater than the border width could be influenced by an intermetallic just outside the image. For example, a pixel right at the border with a value of 50 microns is claiming that there is no intermetallic particle within the first 5 microns outside the image, but there is no way it can know that. Limiting the pixels used for the histograms to those remaining inside the border that have values less than the border with ensures that all data used is confidently correct.

The final microstructural feature of interest obtained from EBSD in this work is the local GND density. As described previously, the local curvature of the orientation field is calculated and used to solve for the L1 norm of Nye's dislocation density tensor [8, 9]. The log GND density is mapped for a scanned region in Figure 21 below. The GND density typically ranged from about 10^{12} to 10^{16} m^{-1}.

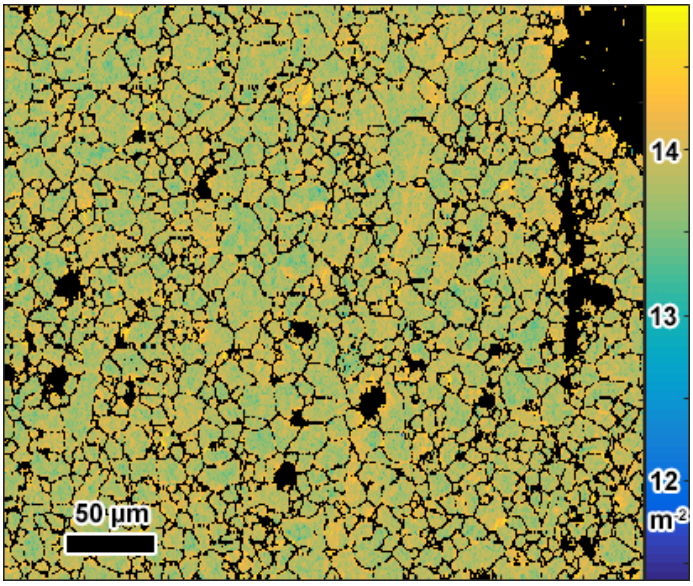

Figure 21: GND density map for a region of interest. Pixels with CI < 0.1 are blacked out.

It was observed that the GND density was higher near intermetallic particles, due to the strain caused by the particle being embedded in the matrix. This could potentially cause an issue in which the effects of the GND density could not be distinguished from those of the intermetallic particles. If increased pitting was observed at higher dislocation densities, one could argue that the pitting was actually due to the intermetallic particles (which happen to have higher GND density around them). GND density could have no effect on pit initiation and yet it might appear that it does because of the coupling between intermetallic particles and higher GND density. Therefore, to mitigate this possibility, the GND density maps were screened before being used to calculate relative pitting histograms. For each map, all pixels within 10 microns of an intermetallic particle were excluded. This is shown below in Figure 22.

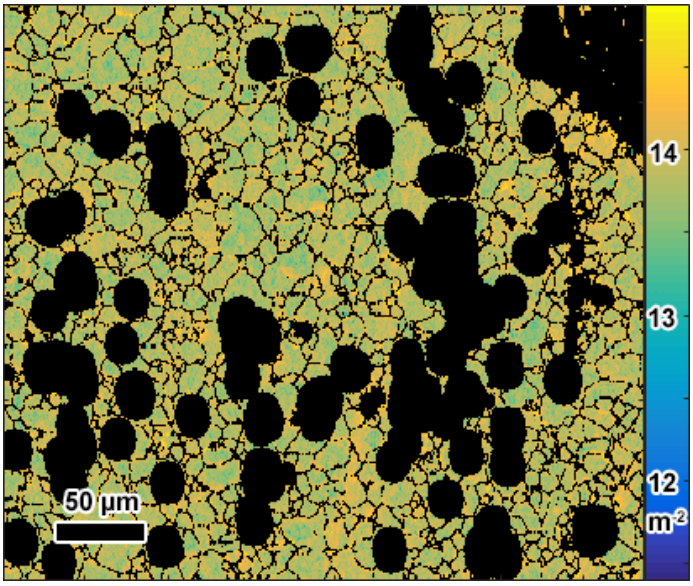

Figure 22: GND density map for a region of interest that has been screened, masking all data within 10 microns of an intermetallic particle. Pixels with CI < 0.1 are blacked out.

When calculating relative pitting histograms as a function of GND density, only pixels more than 10 microns away from any intermetallic particle were used. This distance was chosen based on the intermetallic particle proximity histograms, which showed that beyond roughly 10 microns the intermetallic particle did not significantly influence pit initiation. This effectively separates the contribution of intermetallic particles and GND density, ensuring that any correlations found between GND density and pitting are not artifacts of the influence of intermetallic particles.

For each feature of interest, the goal is to use the binary pit map to mask the different microstructural maps discussed previously in this section in order to obtain microstructure information for every pitted point on the surface. In order to do that, the pit maps must be properly registered or aligned with the EBSD scan data. This is done using the image quality map, shown below in Figure 23.

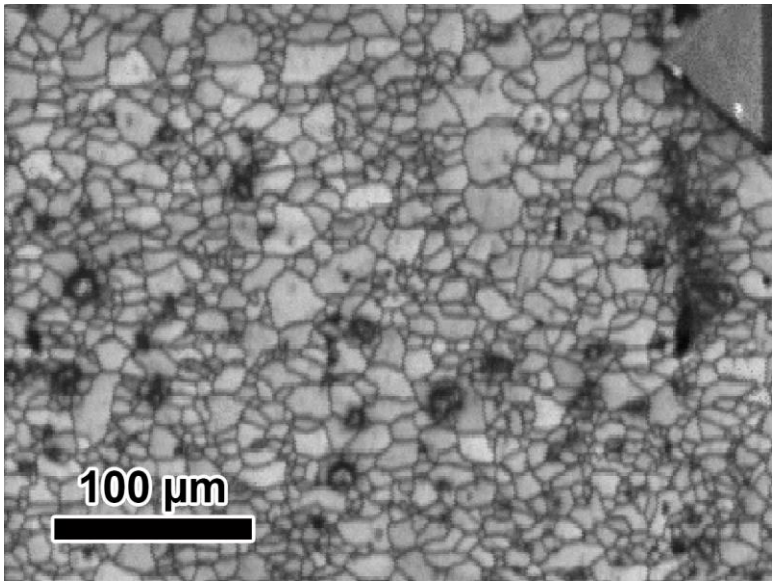

Figure 23: Image quality map from EBSD scan of a region of interest. The image quality map was used to match and align binarized maps to scan data.

The image quality map show is generated directly from EBSD scan data and shows the intermetallic particles and fiducial markers. This means that it can be used in this work to match up point-by-point the EBSD scan data with the pit maps (or binary intermetallic particle maps). Multiple points are selected in the image quality map (usually near intermetallic particles or the fiducial marker for ease of identification) and corresponding points are selected in the pit map. A distortion field is applied to transform the pit map so that the corresponding points are aligned and the pit map shows the same area as the image quality map. This direct correspondence is important for accurately applying the pit maps and ensuring the analysis is comparing the same points. This process is required for both the binary pit map and the binary intermetallic particle maps because they are images and have no EBSD reference. The point-by-point matching with the image quality map puts these images in the context of the EBSD scan data and aligns them with the microstructural

maps. Figure 24 below shows an example of this point-by-point matching between the image quality map and an intermetallic particle map.

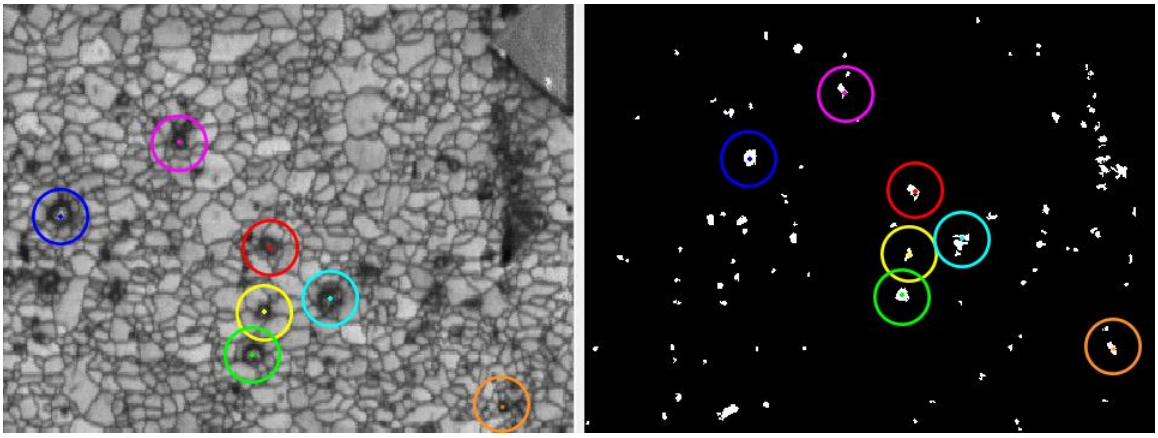

Figure 24: Image quality map (left) and a binarized intermetallic particle map (right) of the same region of interest. Colored circles show corresponding points identified in each map.

4.1.3 Pit Detection

In order to directly tie microstructural features to pitting initiation, microstructural maps needed to be combined with binarized pit maps. These maps show the location of every pitted pixel in the image and can be used to mask the microstructural maps, providing the relevant microstructural information for every pitted point. In order to construct these binarized maps, an automated image processing and pit detection routine was developed in collaboration with P. Fernandez-Zelaia and S.N. Melkote. Figure 25 below shows the processing workflow. First, the image intensity is normalized by subtracting the mean intensity from the image and dividing the result by the standard deviation. This creates a normalized intensity variable locally at every point and helps correct for shadowing as well as giving the pitted regions better contrast with the matrix, particularly in the vicinity of intermetallic particles.

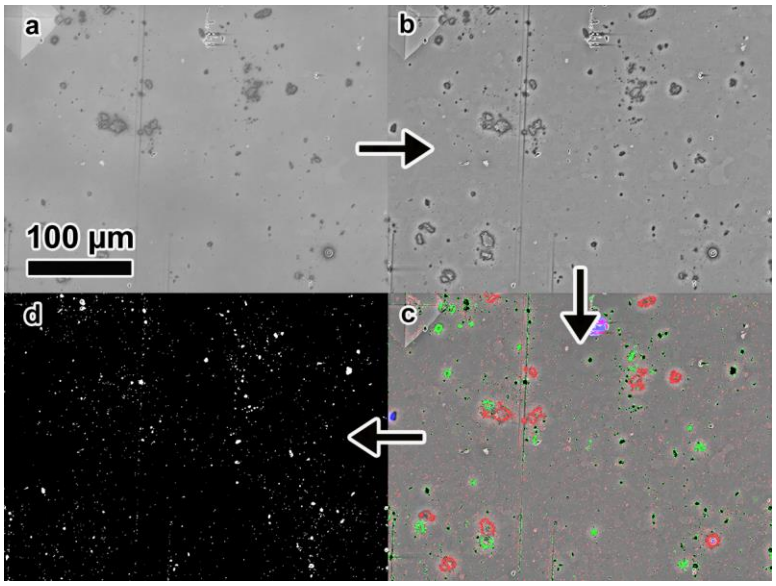

Figure 25: Pit detection workflow. The raw SE image (a) is intensity normalized (b) and domain knowledge is applied (c) to determine which regions should be identified as pits and thresholded to create the final pit map (d). Red regions are excluded based on intensity gradient, while blue regions are excluded base on size. Green regions are accepted to be used for pit detection.

The second step applies domain knowledge of the system to label the various regions of interest before thresholding. Objects above a certain size threshold were excluded since they were larger than an initial pit would be and were more likely a silicon-rich intermetallic particle (making it appear dark in the BSE image). In many cases, iron-rich intermetallics (which appear bright in the BSE image) have a dark edge to them, so these regions are excluded as well based on intensity gradient since the dark appearance is from the intermetallic edge and not a pit. Applying these types of domain knowledge exclusions help ensure that, in the final step, the edge detection and intensity thresholding only captures the desired pitting phenomenon and the final binarized pit map accurately shows pit initiation sites. This threshold was selected manually based on intensity for the pits in the normalized image.

Figure 26 below highlights the end result of this pit detection process by comparing side-by-side the raw SE image from Figure 25 and the final binarized pit map. Manual comparison of the raw SE image with the final binarized pit map showed good agreement, with nearly all of the pit initiation sites correctly identified. The pit maps were then aligned with the microstructural maps to ensure that an accurate overlay and masking could be performed. Multiple points were selected in the image quality map from the EBSD scan and corresponding points were selected in the binarized pit map (points were typically chosen near a fiducial indent or intermetallic particle for ease of identification), then a distortion field was applied to match the selected points and align the image. This same alignment process was used for binarized intermetallic maps as well, since the map needed to be overlayed with EBSD scan data in order to draw correlations. After the pit maps were appropriately aligned, they were used to mask the microstructural maps shown earlier in this section. In this way, the grain orientation, grain boundary proximity, intermetallic particle proximity, and GND density was identified for every pitted point on the sample surface.

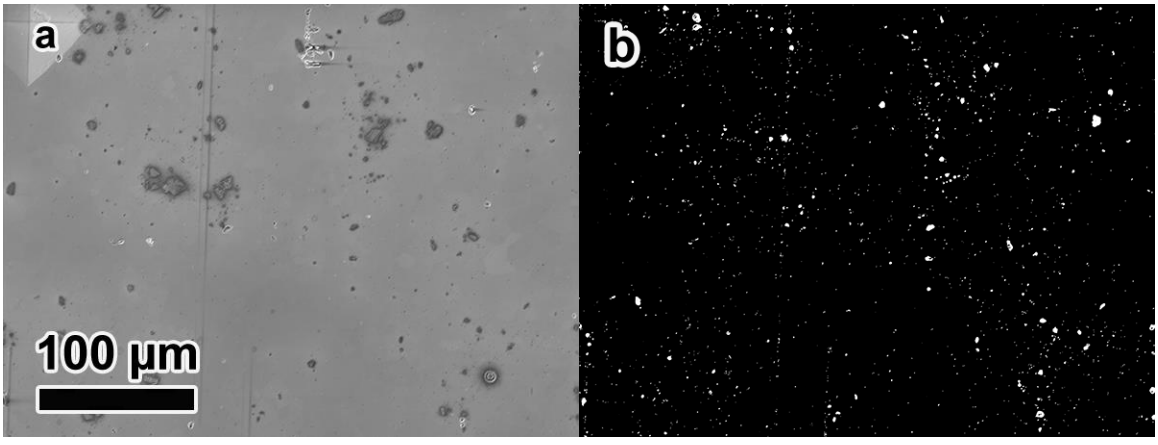

Figure 26: Comparison of raw SE image and final binarized pit map.

The first two major parts of the analysis have been completed: detailed microstructural characterization has been performed (providing details on the three microstructural features of interest) and the automated pit detection has been carried out so that this microstructural information can be correlated with pitting initiation sites. What follows is an analysis of the pitting frequency as a function of grain orientation, intermetallic particle proximity, grain boundary proximity, and GND density in order to build first-order correlations between the pitting initiation behavior and the local microstructure.

4.2 Mesoscale Characterization and Corrosion of Unsensitized AA5083

Prior to exposure to the NaCl solution, detailed microstructural analysis was performed to characterize grain size, grain orientation, grain boundary state, intermetallic particle distribution, and GND density. All but one of these features (intermetallic particle distribution) come directly from EBSD mapping, shown below in Figures 27-29.

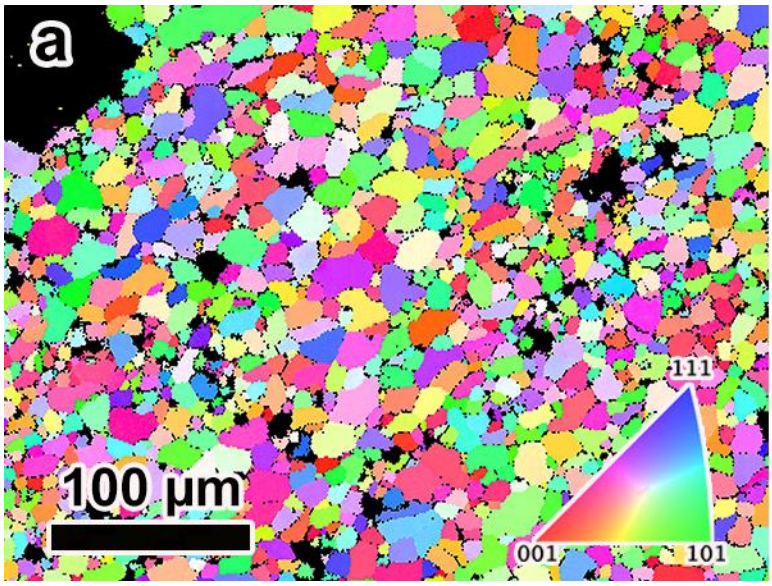

Figure 27: IPF map for a 70% cold rolled region of interest. Pixels with CI<0.1 are blacked out. An IPF triangle shows the color key for orientation.

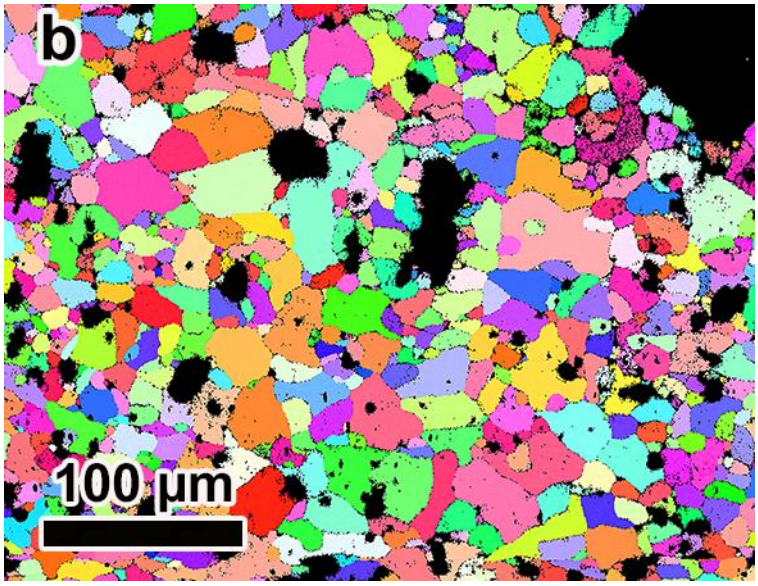

Figure 28: IPF map for a 50% cold rolled region of interest. Pixels with CI<0.1 are blacked out.

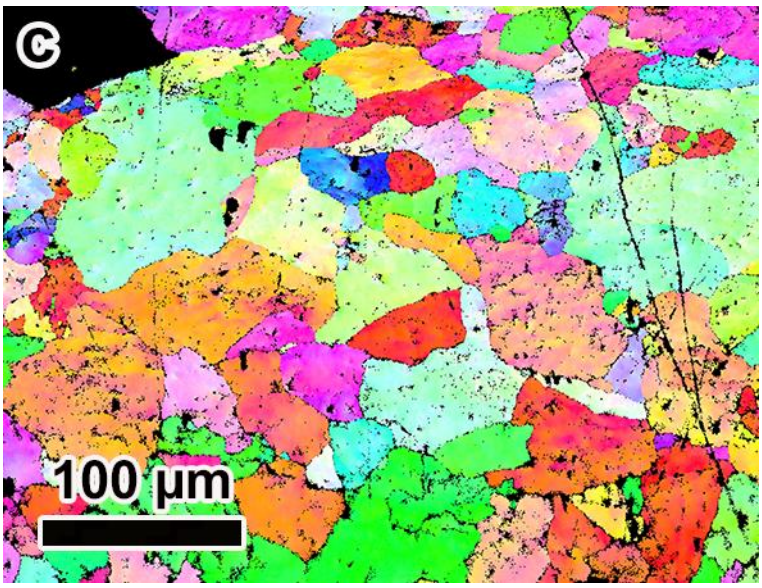

Figure 29: IPF map for an as-received region of interest. Pixels with CI<0.1 are blacked out.

4.2.1 Grain Orientation

The cold rolled and annealed samples showed a more uniform grain structure than the as-received samples, as well as reduced grain size. The average grain size (diameter) for the as-received, 50% cold rolled, and 70% cold rolled samples were approximately 45 µm, 20 µm, and 15 µm, respectively. The IPF maps in Figures 27-29 do not show a show a strong texture. This was confirmed by performing a texture analysis on the entire scanned area for each sample condition. The results of the sum-total texture analysis are shown below in Figures 30-35 for the 70% cold rolled condition, 50% cold rolled condition, and the as-received condition, respectively, before and after corrosion.

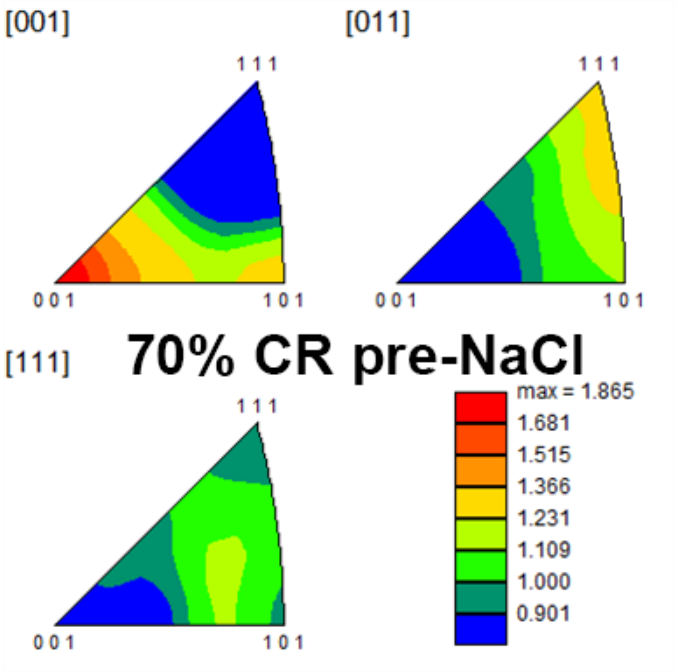

Figure 30: IPFs from texture analysis of 70% cold rolled samples prior to corrosion, showing three reference directions. The colorbar units are in times random.

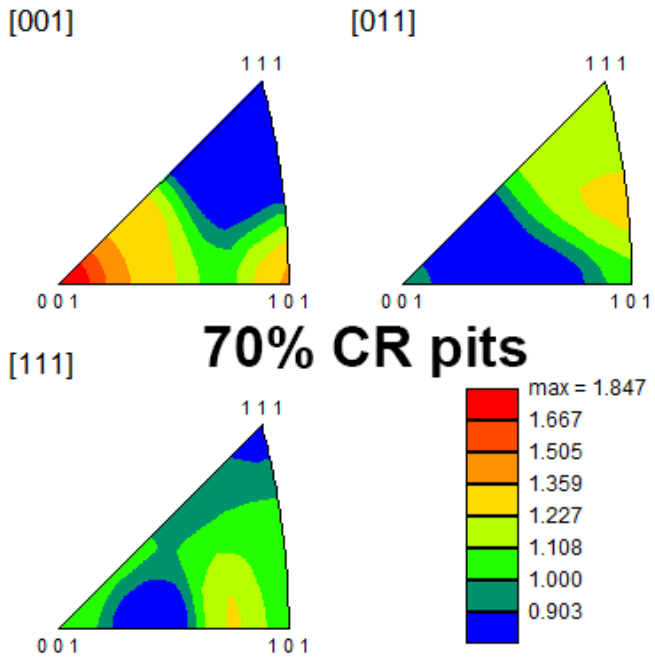

Figure 31: IPFs from texture analysis of all the pitted points for the 70% cold rolled samples, showing three reference directions. The colorbar units are in times random.

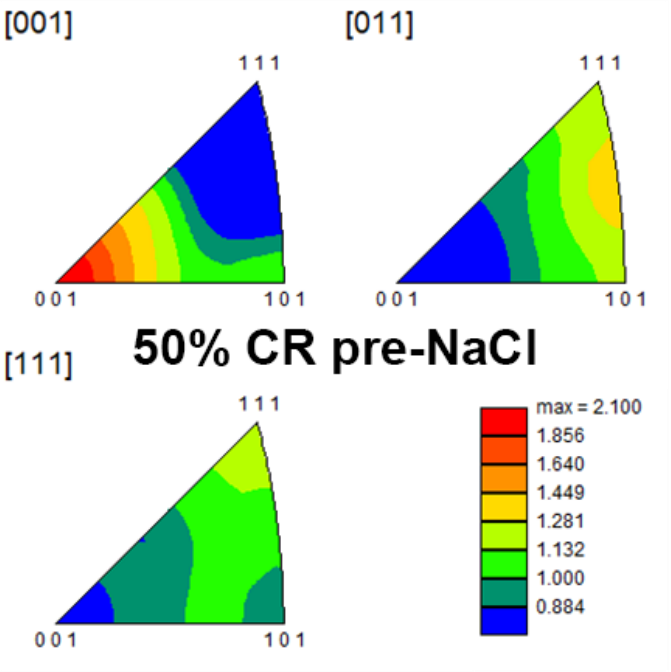

Figure 32: IPFs from texture analysis of 50% cold rolled samples prior to corrosion, showing three reference directions. The colorbar units are in times random.

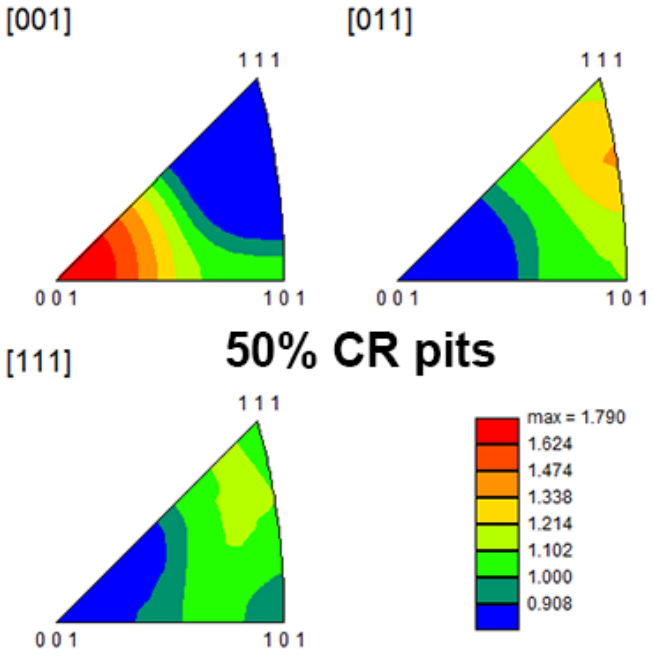

Figure 33: IPFs from texture analysis of all the pitted points for the 50% cold rolled samples, showing three reference directions. The colorbar units are in times random.

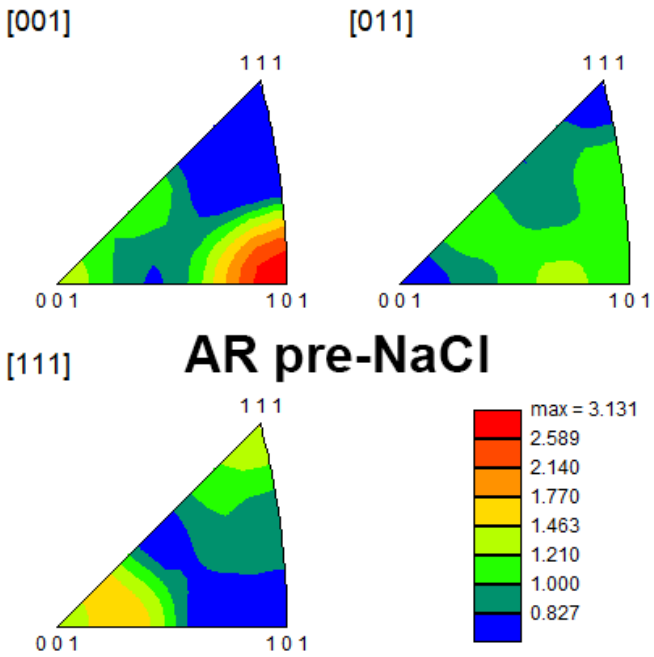

Figure 34: IPFs from texture analysis of the as-received samples prior to corrosion, showing three reference directions. The colorbar units are in times random.

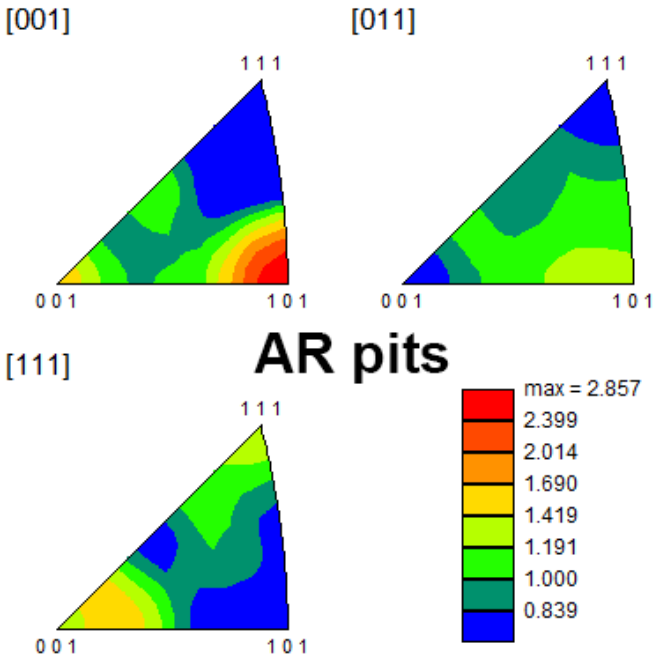

Figure 35: IPFs from texture analysis of all the pitted points for the as-received samples, showing three reference directions. The colorbar units are in times random.

Figures 30, 32, and 34 above show the texture of the uncorroded samples prior to corrosion. The color bar is in units of times random. The three IPFs each have a different sample axis, given in brackets, and the plots show what crystallographic directions are parallel to that axis, labeled at the three corners of the triangle. The IPFs indicate that there is not particularly strong texture in the samples, with the maximum intensity being 3.1 times random as opposed to something like 5 times random or more. This texture analysis created a baseline against which the texture analysis of the pitted pixels could be compared.

In order to study the correlation between grain orientation and pitting, texture analysis was also performed on all the pitted pixels in each sample condition. By combining EBSD scan data with binarized pit maps, the grain orientation (prior to corrosion) of every pixel that became pitted was known. This meant the texture of the pitted pixels could be analyzed to look for trends between grain orientation and pitting initiation. Figures 31, 33, and 35 above show the IPFs of the pitted pixels for all three sample conditions, counterparts to Figures 30, 32, and 34.

The IPFs of the pitted points are quite similar to the pre-corroded IPFs, and still do not show a particularly strong texture. For the 70% cold rolled samples, the maximum intensity changed from 1.86 to 1.85 times random and the highest and lowest intensities were in the same orientations for the pits as for the uncorroded samples. For the 50% cold rolled samples, the plots also looked almost identical and the maximum intensity only changed from 2.10 to 1.79 times random. Finally, the as-received plots also look nearly identical and the maximum intensity only changed from 3.13 to 2.86 times random. None of the sample conditions showed a pitting texture that was largely different from the pre-corroded sample texture. The orientations with higher or lower concentrations remained

unchanged between the pre-corroded samples and the pits, showing that the pits were essentially a random uniform selection of the available orientations.

Although some work in the literature showed a correlation between grain orientation and pitting resistance, no such correlation was seen in this work. This could be because this work focused on pit initiation, so perhaps grain orientation does not strongly affect initiation but does affect pit growth. It could also be that some other secondary factor besides grain orientation was responsible for the changes in pitting resistance seen in the literature, and that factor was not distinguished from grain orientation. These discrepancies highlight the need to understand the interplay of multiple microstructural features with each other when determining their influence on corrosion behavior. Further investigation of the effect of grain orientation on pitting behavior is clearly needed.

4.2.2 Intermetallic Particle Proximity

The microstructural maps from Section 4.2 were combined with the binarized pit maps illustrated in Figure 26 so that, for every pitted pixel in the image, the values for intermetallic particle proximity, grain boundary proximity, and GND density were known. For each of the three sample conditions (as-received, 50% cold rolled, and 70% cold rolled), normalized frequency histograms were created showing the relative pitting frequency as a function of each of the three microstructural features of interest. Each bin of the histogram shows the number of pitted pixels for that distance divided by the total number of the pixels in the image for that distance, thus normalizing each bin to show the relative percentage of the total number of pixels that had been pitted. For example, if the histogram for intermetallic particle proximity showed a value of 2% at a distance of 5 μm,

that means that of all the pixels in the image that were 5 μm away from the nearest intermetallic, 2% of them were pitted. Such normalization is important when developing these trends as a function of microstructure, since in cases like the 70% rolled case where the vast majority of the population are short distances away from grain boundaries, absolute frequency depictions would be quite skewed. The frequency histograms for the noble intermetallic particle proximity are shown below in Figures 36. Each figure shows the approximate area that was sampled for the statistics, so that considerations of sampling size and associated limitations could be included in the discussion. Error bars show the standard error for each bar of the histogram, being the standard deviation across all regions divided by the square root of the number of regions.

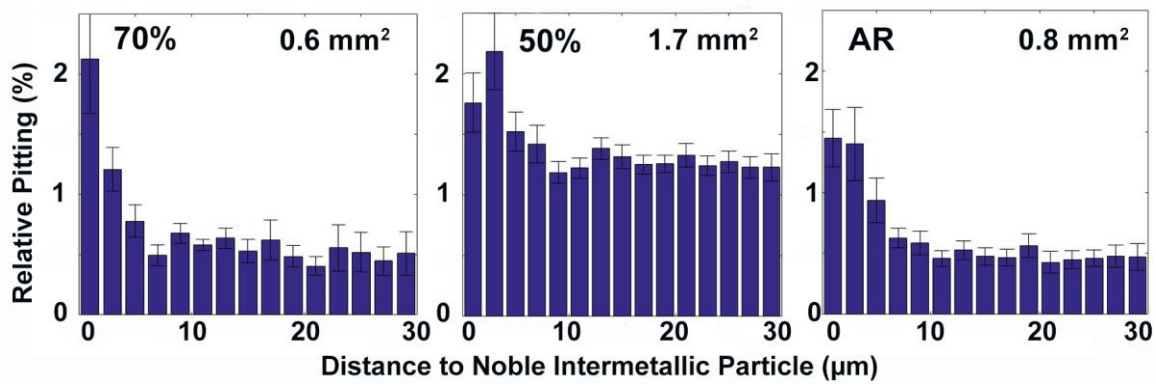

Figure 36: Relative pitting histograms for each sample condition as a function of distance to the nearest noble intermetallic particle. The amount of surface area investigated for each condition is also shown.

For all three sample conditions, the relative pitting increases closer to noble intermetallic particles. The pitting frequency is highest very close to the noble particles and then decreases sharply within a few microns. Further away than roughly 10 microns, the pitting frequency remains relatively unchanged with increasing distance from the noble particle. This is in line with the discussion of galvanic corrosion in Chapter 2: the

intermetallic particle that is noble relative to the matrix induces pitting in that matrix, but this effect diminishes with distance from the particle as ionic transport must reach further and further. This is also supported in the literature in work by Yasakau et al. measuring the Volta potential at and near different intermetallic particles in AA5083 in an NaCl solution [33]. The authors found that the Volta potential differed at and near the intermetallic particles, but this effect was reduced as distance from the particle increased [33]. Although they did not directly comment on the range of this effect, the plots showed that it seemed to be similar to what is observed in this work (on the order of roughly 10 microns). The histograms above in Figure 36 show a clear trend in which pitting increases closer to the noble intermetallic particle.

The population of active intermetallic particles observed in this work was quite small compared to noble intermetallics. In most cases, there were too few active particles to enable binarized intermetallic maps to be matched and aligned with the EBSD scan data. Such an example is shown below in Figure 37, where only a couple of active particles are seen in the entire scanned region.

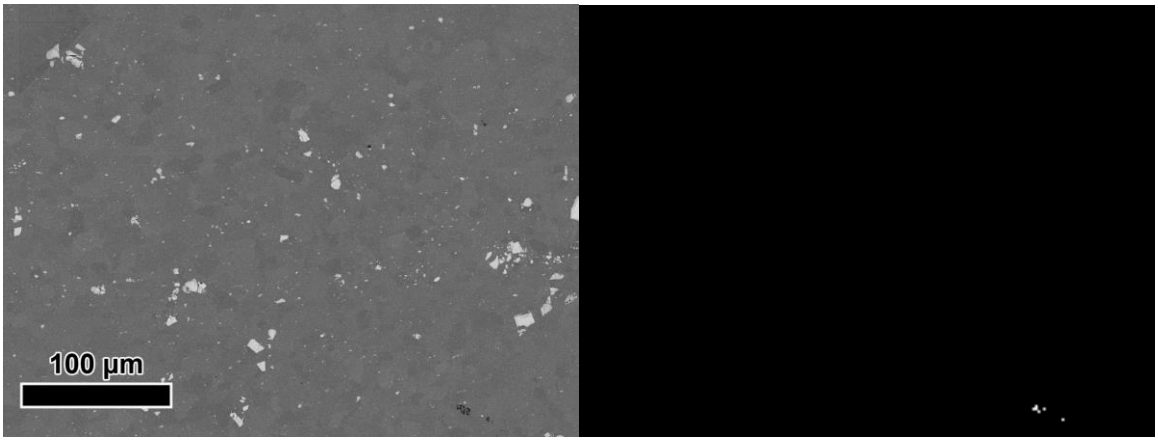

Figure 37: Raw BSE image (left) and binarized active intermetallic map (right) for a region of interest, highlighting the low population of active particles.

The few cases that had enough active intermetallics to enable matching with the EBSD scan data did not amount to enough regions to calculate confident statistics. Therefore, for this work, active intermetallic particles are not analyzed in terms of their impact on pitting initiation. Future studies will have to change the way active intermetallics are examined, most likely by changing the way the region of interest is determined. Instead of analyzing large areas that may only have few active particles, perhaps each scanned region will center on one active intermetallic. This would mean each scanned region would investigate the vicinity of one active particle to see how pitting initiation changed with distance. Alternatively, regions could be selected in a similar manner to this work and the scanned region can just be made larger. However, if the imaged region becomes too large there is a loss of image resolution that can make matching binarized maps difficult.

4.2.3 GND Density

A correlation between relative pitting and local GND density was also seen in all three sample conditions (Fig. 38). As the GND density increased, so did the pitting

frequency. It could be that dislocation clusters are higher energy sites that destabilize the passive film, or there could be chemical segregation taking place there. The influence of local GND density on pit initiation has not been widely reported in the literature, so this finding helps broaden our understanding of the interplay of multiple microstructural features in determining the corrosion susceptibility of a material and merits further investigation.

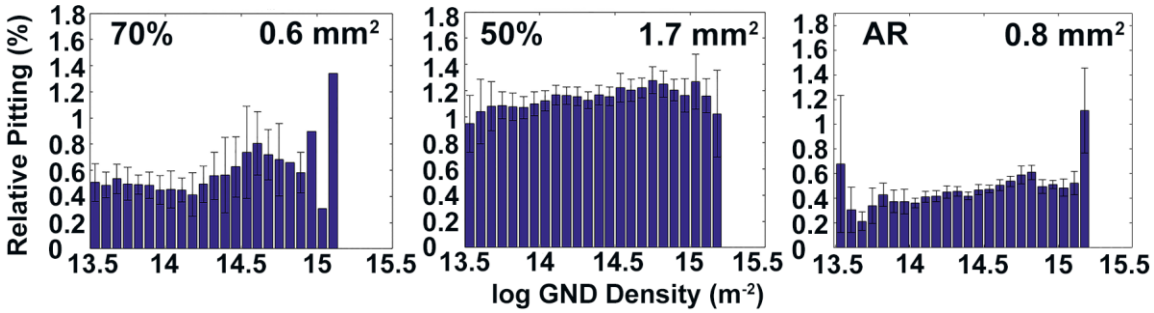

Figure 38: Relative pitting histograms for each sample condition as a function of log GND density. The amount of surface area investigated for each condition is also shown.

This effect is small, however, no more than 1% in any of the sample conditions. It is unlikely that this effect would outweigh the contribution of intermetallic particles in determining the pitting susceptibility of the region. The total population of points with very low GND density or very high GND density was quite low, and this can be seen in the increased uncertainty and sometimes sporadic values at either end of the histograms (tails). Bins with no error bars had exceedingly high error that, if given, would make the rest of the histogram difficult to read. However, data in the middle ranges of GND density (with less uncertainty) do show the trend. Although small, the effect does seem to be consistent, showing increased relative pitting with increased GND density.

4.2.4 Grain Boundary Proximity

The final microstructural feature studied in this work was grain boundary proximity. No clear correlation was seen, for any sample condition, between relative pitting and distance to nearest grain boundary (Fig. 39).

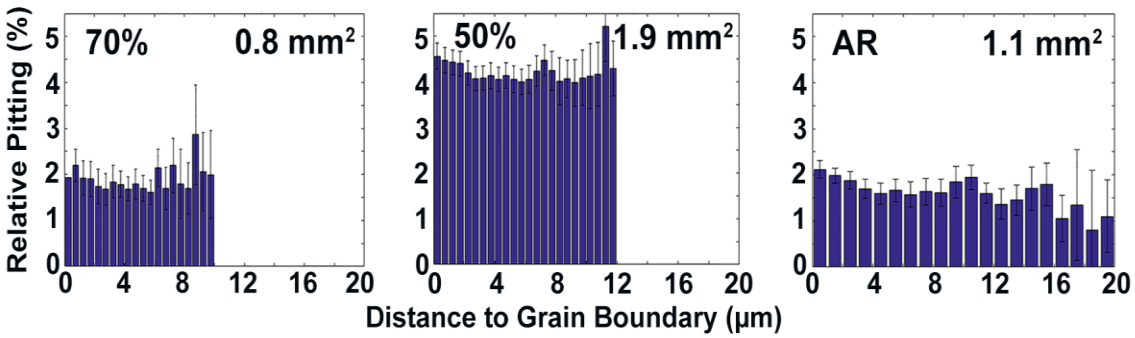

Figure 39: Relative pitting histograms for each sample condition as a function of distance to the nearest grain boundary. The amount of surface area investigated for each condition is also shown.

The pitting frequency remains relatively unchanged as a function of distance to grain boundary. Once again, some sporadic values with increased uncertainty are seen at higher distance values because the population of such points is relatively low. There are several possibilities for the lack of correlation seen in the grain boundary proximity histograms. It could be that grain boundary proximity does not affect pit initiation, or that the effect is small enough that it is dwarfed by other microstructural features. It could be that more sampling is needed to fill out the statistics, meaning that the current data is not enough for a trend to form. However, the histograms look similar for both the 70% cold rolled case and the 50% cold rolled case, even though they have very different amounts of data. This makes it somewhat less likely that simply more data is needed. Another possibility is that the lack of correlation stems from a limitation of the analysis: all grain

boundaries are treated the same. Grain boundaries were not split into such categories as low-angle, high-angle, or coincident site lattice boundaries. It could be that there are competing effects from different types of grain boundaries and these effects mask any correlation in the histograms. Future refinement of the analysis toolset will need to take into consideration different types of grain boundaries to determine if there is any correlation with pitting initiation.

4.3 Mesoscale Characterization and Corrosion of Sensitized AA5083

The analysis from the previous section was also performed for sensitized AA5083 samples. These samples were sensitized at 175 °C for 72 hours, inducing the precipitation of β phase. Past work in the literature has shown that sensitization should not affect any of the other microstructural features of interest studied in this work, but the presence of β-phase particles could possibly affect how those feature impact pitting initiation. To quantify the degree of sensitization of the samples, nitric acid mass loss testing (NAMLT) was performed. As-received unsensitized samples were measured as a baseline, then all three conditions of sensitized samples (70% cold rolled, 50% cold rolled, and as-received) were measured. The results of the NAMLT measurements are given in Table 3 below.

Table 3: Results of NAMLT for all three sensitized conditions and one unsensitized baseline condition.

Sample	Approx. Area (mm^2)	Mass Difference (g)	NAMLT (mg/cm^2)
AR	577.03	0.101	17.50
AR	536.17	0.083	15.48

Table 3 continued.

Sample	Approx. Area (mm^2)	Mass Difference (g)	NAMLT (mg/cm^2)
AR 72	566.62	0.265	46.76
AR 72	560.08	0.251	44.81
50CR 72	488.50	0.120	24.57
50CR 72	421.62	0.141	33.44
70CR 72	807.63	0.222	27.49
70CR 72	668.52	0.182	27.22

The unsensitized baseline condition showed a NAMLT value of roughly 16 mg/cm^2, whereas the sensitized samples showed significantly higher values. The sensitized 70% cold rolled condition, 50% cold rolled condition, and as-received condition showed NAMLT values of roughly 27 mg/cm^2, 30 mg/cm^2, and 45 mg/cm^2, respectively. The reduction is NAMLT value for the cold rolled and annealed samples agrees with the work in the literature by Tan and Allen [32]. However, the effect of thermomechanical treatment on degree of sensitization is not the focus of this work. Rather, the goal here was to investigate how the presence of the β phase might play a role in how the microstructural features of interest affected pitting initiation. Therefore, the same kind of analysis of texture, noble intermetallic particle proximity, grain boundary proximity, and local GND density was performed for the sensitized samples.

4.3.1 Grain Orientation

The IPFs showing the texture analysis for the sensitized samples are shown below in Figures 40-45, showing all three sample conditions before and after corrosion.

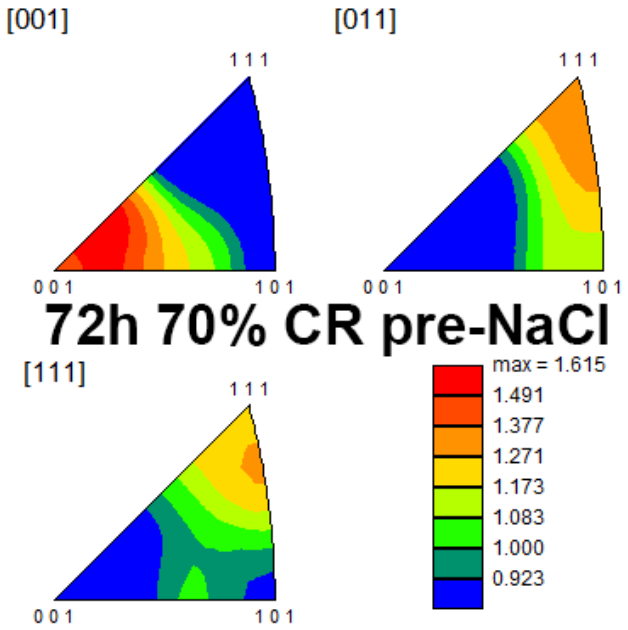

Figure 40: IPFs from texture analysis of 72-hour sensitized, 70% cold rolled samples prior to corrosion, showing three reference directions. The colorbar units are in times random.

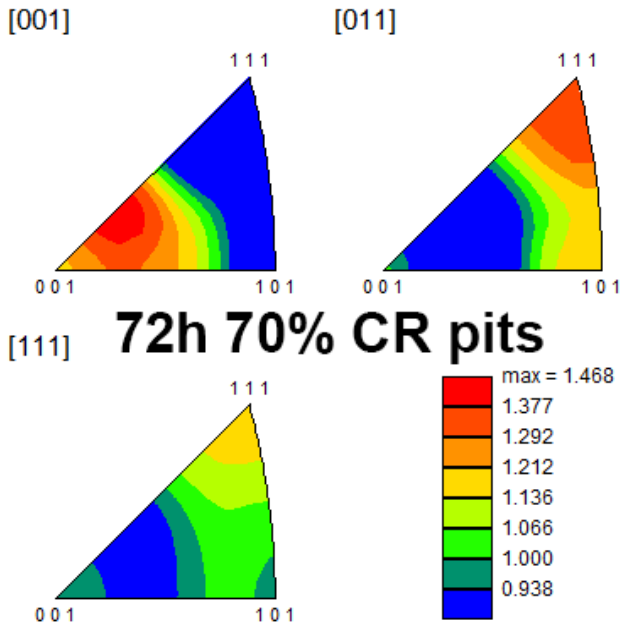

Figure 41: IPFs from texture analysis of all the pitted points for the 72-hour sensitized, 70% cold rolled samples, showing three reference directions. The colorbar units are in times random.

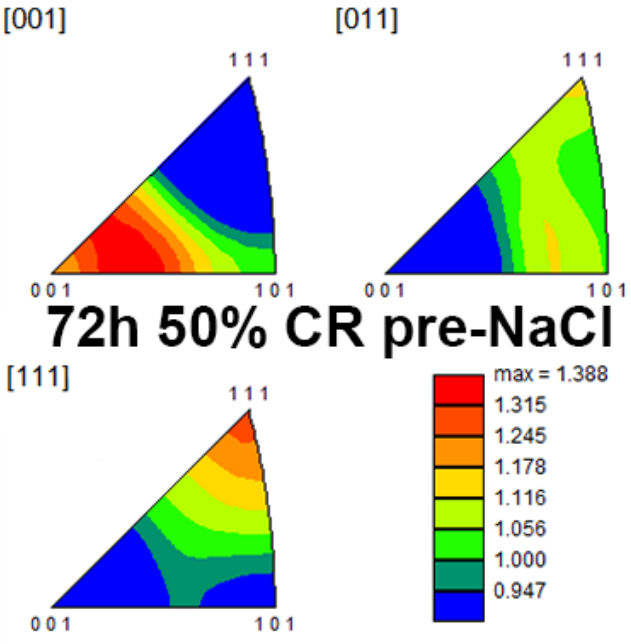

Figure 42: IPFs from texture analysis of 72-hour sensitized, 50% cold rolled samples prior to corrosion, showing three reference directions. The colorbar units are in times random.

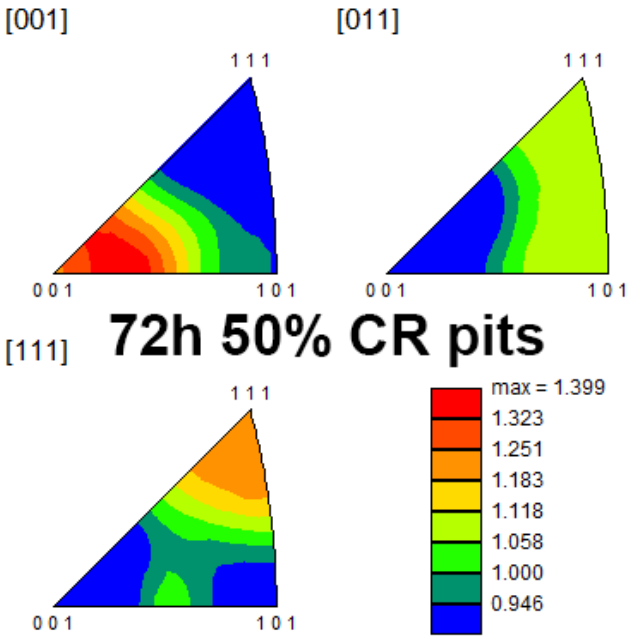

Figure 43: IPFs from texture analysis of all the pitted points for the 72-hour sensitized, 50% cold rolled samples, showing three reference directions. The colorbar units are in times random.

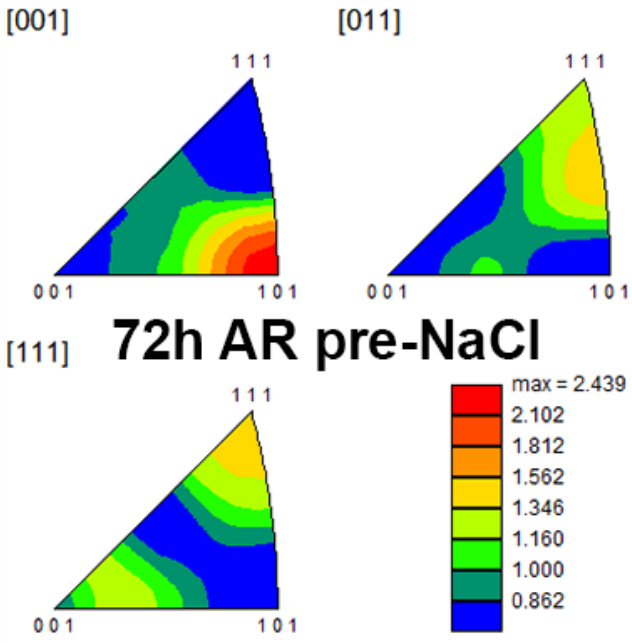

Figure 44: IPFs from texture analysis of the 72-hour sensitized, as-received samples prior to corrosion, showing three reference directions. The colorbar units are in times random.

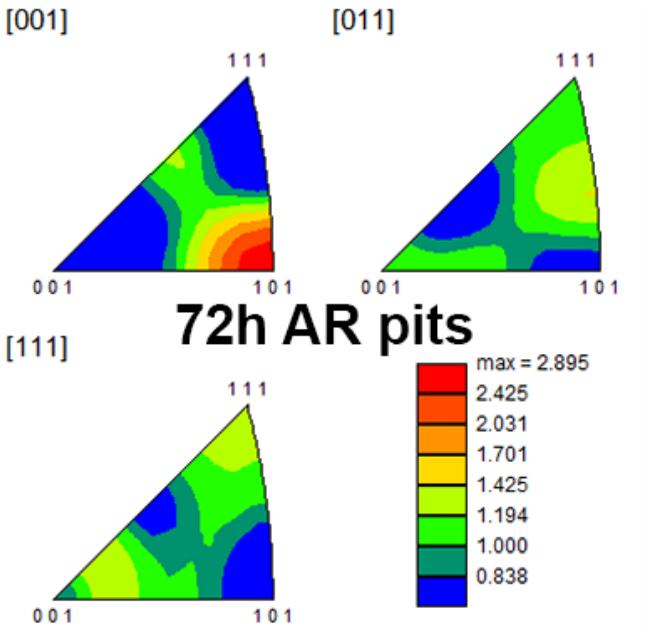

Figure 45: IPFs from texture analysis of all the pitted points for the 72-hour sensitized, as-received samples, showing three reference directions. The colorbar units are in times random.

As with the unsensitized samples, the pre-corrosion IPFs (Figs. 40, 42, 44) did not show a strong texture for any of the conditions. Once again, the as-received condition showed the highest intensity (2.4 times random) since the grains are larger and therefore fewer grains are included in the texture analysis. The IPFs for the pitted points in all three sample conditions are shown in Figures 41, 43, and 45 for comparison.

Once again, the IPFs for the pitted points are nearly identical to those of the uncorroded samples. For the 70% cold rolled case, the maximum intensity changed from 1.62 to 1.47. For the 50% rolled case, the maximum changed from 1.39 to 1.40. For the as-received case, the maximum changed from 2.90 to 2.44. For all three conditions, the orientations with the highest and lowest concentrations were practically unchanged between the pitted points and the uncorroded baseline. This indicates that the pits initiated

essentially uniformly from all available orientations, showing that there was no strong correlation between grain orientation and pit initiation.

4.3.2 Intermetallic Particle Proximity

The relative pitting histograms as a function of distance to the nearest noble intermetallic are shown in Figure 46 below. Once again, the relative pitting percentage is shown for each sample condition and the investigated area is indicated.

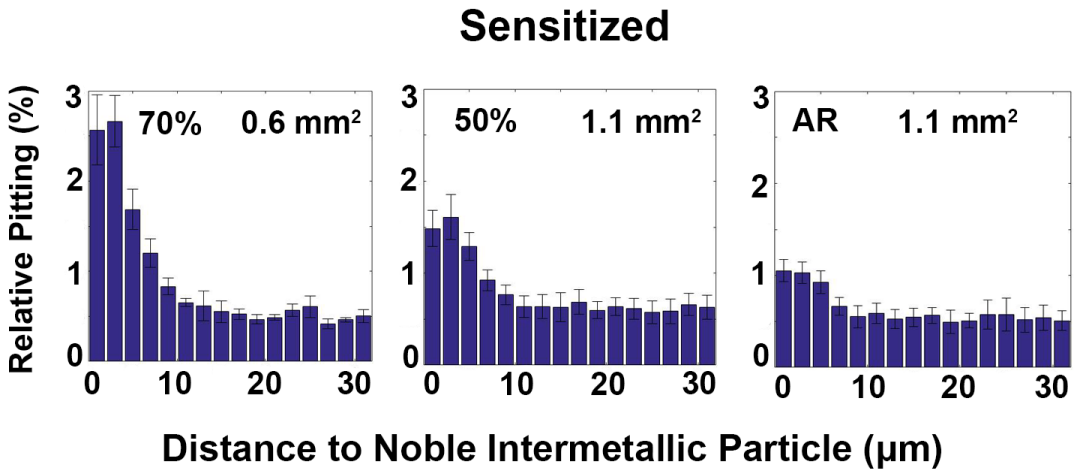

Figure 46: Relative pitting histograms for each sensitized sample condition as a function of distance to the nearest noble intermetallic particle. The amount of surface area investigated for each condition is also shown.

As in the unsensitized case, relative pitting increased closer to noble intermetallics, and the effect appears slightly more prominent than for the unsensitized case. Even more so, however, is the difference between sensitized conditions. The 70% cold rolled condition shows a much more prominent effect than the 50% cold rolled or as-received conditions. This could be related to the grain size reduction from cold rolling. The smaller grain size

condition has a greater total grain boundary length, and the grain boundaries contain β-phase that shifts the nearby region to more anodic potentials, so this could create a larger galvanic driving force between the noble intermetallics and the matrix. This increase galvanic driving force would induce more pitting in the matrix near noble intermetallics. This would also account for the increase in the effect in sensitized samples versus unsensitized. However, it remains unclear why the decrease in relative pitting for the as-received case is so gradual compared to the unsensitized as-received condition. Further work is needed to provide further insight into the cause of these apparent differences in pitting behavior, possibly looking more closely at the interplay between grain boundaries and intermetallic particles.

4.3.3 GND Density

For the histograms showing relative pitting as a function of GND density, there appears to be a trend in the 70% cold worked condition showing increasing pitting with increasing GND density. For the other two conditions, there is not a clear trend, especially due to larger uncertainty at higher GND density values These histograms are shown in Figure 47 below.

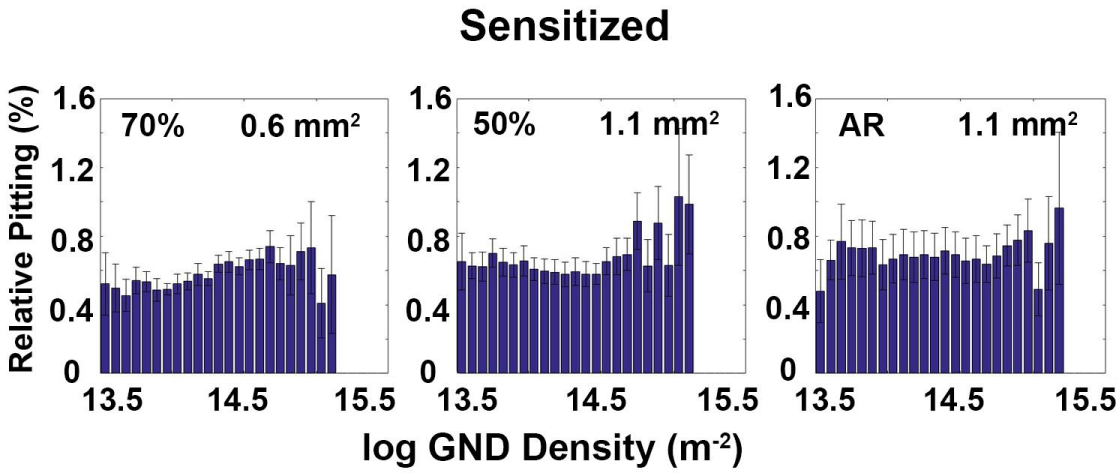

Figure 47**: Relative pitting histograms for each sensitized sample condition as a function of log GND density. The amount of surface area investigated for each condition is also shown.**

As in the unsensitized case, this effect is small. However, tails on either end of the histograms show greater uncertainty (because the population of very high and very low GND values is small) and may be creating an artifact. For both unsensitized and sensitized cases, further investigation is needed to show whether pit initiation increases with GND density. This work does, however, build the framework for just such investigations to be continued and refined.

4.3.4 Grain Boundary Proximity

The histograms showing relative pitting as a function of distance to nearest grain boundary are given below in Figure 48. Once again, there does not seem to be a clear trend. None of the values that have a relatively small uncertainty vary more than half a percent or so, and for some conditions pitting seems to decrease with distance and for others it appears to increase.

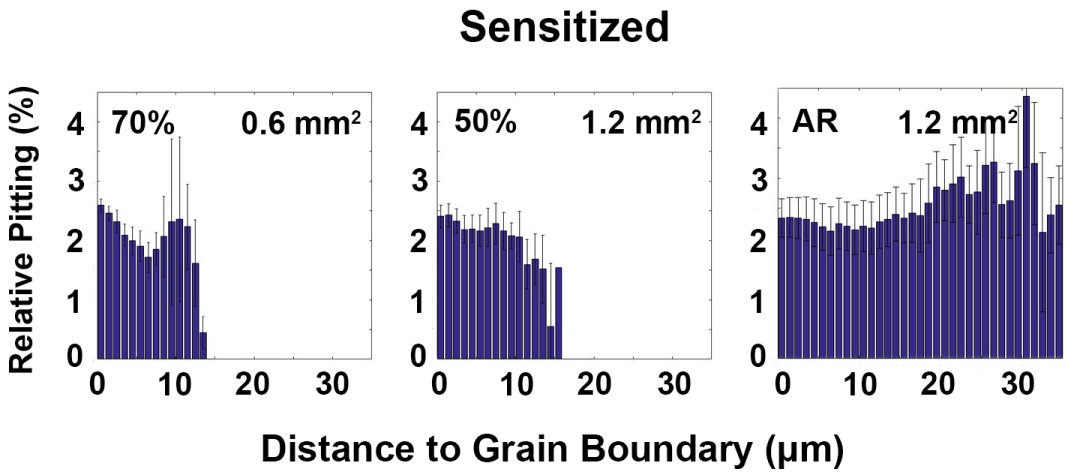

Figure 48**: Relative pitting histograms for each sensitized sample condition as a function of distance to the nearest grain boundary. The amount of surface area investigated for each condition is also shown.**

The 70% cold rolled condition is the only one that shows a consistent change with a small error, showing a stead decrease in pitting for roughly 5 microns. The other two conditions show little change except for when the histograms have large error bars. The trend seen in the 70% condition could be due to the increased grain boundary density and the presence of β phase from sensitization; however, there is only half as much data for the 70% cold rolled condition as the other two. This means the trend could be an artifact of needing more data for the statistics. These results show that further work is needed to investigate the effects of grain boundary proximity. The refinements mentioned in the previous section (categorizing different kinds of grain boundaries) will be helpful in providing insight, as will increasing the number of samples investigated. The work presented here established the framework for these refined investigations and examined the effect of several other microstructural features on pit initiation.

CHAPTER 5. NANOSCALE CORROSION INVESTIGATIONS

5.1 Motivation and Background

Corrosion continues to be an important issue, affecting nearly every industry and costing the global economy an estimated $2.5 trillion annually [6]. Due to the complexity of corrosion mechanisms and the difficulty in directly monitoring corrosion processes at relevant time and length scales, several fundamental processes that govern corrosion behavior remain unresolved. This is especially true for localized corrosion events, where the scale at which corrosion damage initiates, which is on the order of nanometers, and the rate at which corrosion fronts expand into the surrounding matrix make it difficult to determine corrosion initiation processes using conventional post mortem imaging alone [18]. Susceptibility to localized corrosion is known to be dependent on external environmental factors such as temperature and flow rates, surface conditions, and internal microstructural factors, including second phase distribution, grain boundary state, defect populations, and texture [17, 18, 68]. However, rapid expansion of the corrosion front from the initial attack site can obscure the direct identification of factors dictating the local susceptibility in post mortem analysis [17, 69, 70]. For example, work by Jain et al. investigating the corrosion of a sensitized Al-Mg alloy showed that the initiation of localized corrosion can trigger the spread of corrosion to the surrounding region, highlighting the importance of capturing the initial corrosion event [71].

A limited number of studies have applied LC-TEM to understanding localized corrosion processes both with and without potentiostatic control [58, 59, 62, 72-74]. Schilling et al. investigate the influence of the electron beam on potentiostatic measurements and found that the beam current and liquid flow affect the open circuit potential measurements, though the beam-induced effects were found to reach equilibrium with time [72]. Park et al. investigated localized corrosion processes in a range of material/electrolyte systems with and without potentiostatic control and found that beam effects were minimal as long as low-dose protocols were followed [73]. Chee et al. characterized the localized pitting behavior of Al thin films in salt water environments with and without Au implantation and found that pitting events could be directly observed and correlated with ion-irradiated regions [58]. By observing the corrosion behavior of annealed and unannealed Fe thin films in acetic acid, Gross et al. showed that the corrosion resistance increased markedly with increasing grain size [62]. They also observed that corrosion attack occurred preferentially near abnormally grown grains, suggesting the influence of microgalvanic effects.

This work presents dynamic observations of oxidation initiation and propagation events observed in nanocrystalline Fe thin films in a water vapor environment. The first subsection of the results discusses qualitative observations of the oxidation processes. In the second subsection, the focus is on the development of feature recognition and image analysis processes to characterize real- and diffraction-space structural and morphological changes during active oxidation events. This approach is motivated by the large increase in data collection rates associated with the transition from charged coupled device (CCD)

electron detectors to complementary metal-oxide-semiconductor (CMOS) detectors, which enable higher electron sensitivity and significantly faster image collection rates [60].

5.2 Results

5.2.1 Pre-Oxidation Characterization

Prior to conducting a leak check of the liquid cell holder, and thereby exposing the films to an aqueous environment, the microfluidic ports for the liquid cell holder were sealed and the films were characterized in terms of their initial structure and chemistry under vacuum conditions. BF and CDF TEM imaging showed that the initial film was uniform, with a grain size on the order of 10-20 nm (Fig. 49a-c). Microcracking is evident in the film (Fig. 49b), presumably due to interfacial stresses induced during the sputtering process between the Fe film and the Si_3N_4 membrane. These microcracks are more apparent in the annular dark field STEM image showed in Figure 49e. Microcracks were not observed to have a strong influence on the oxidation initiation and propagation, possibly because the grain size is much smaller than the length scale of the microcracks. Selected-area diffraction patterns showed only solid rings, suggesting that the nanocrystalline film did not contain any strong texture components (Fig. 49d). EELS analysis did not reveal any significant Fe oxide presence prior to testing (Fig. 49f).

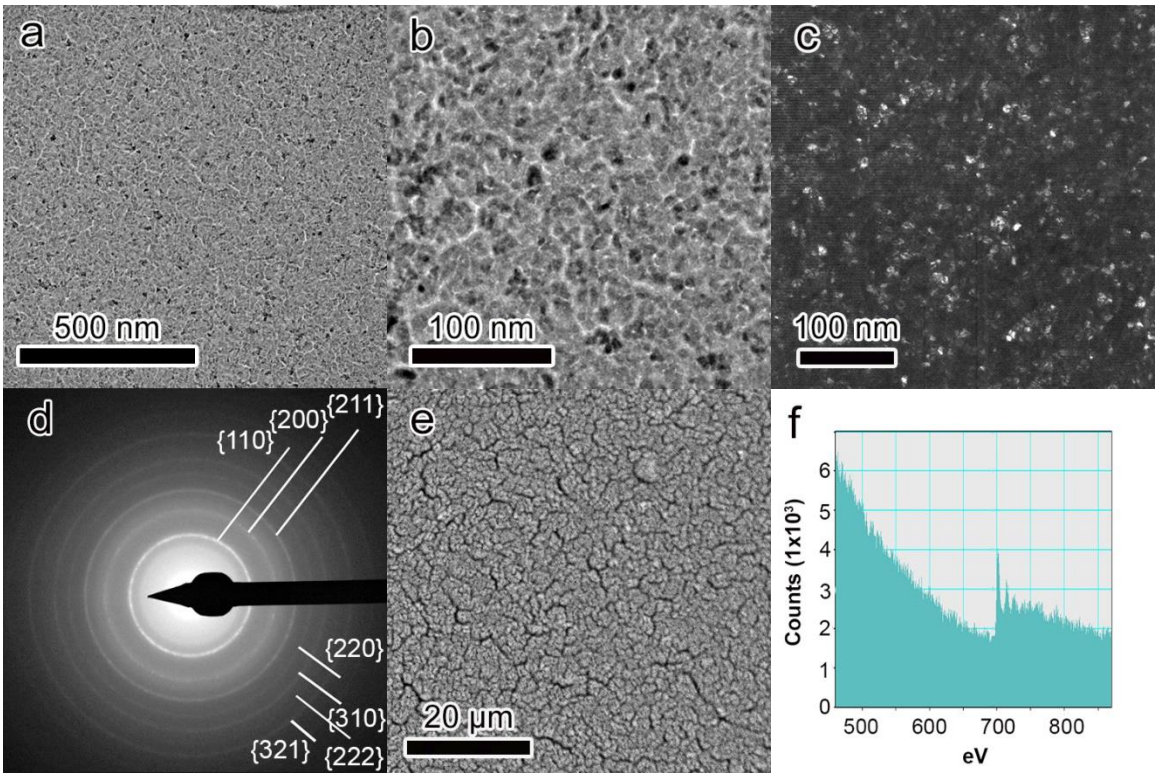

Figure 49: BF TEM analysis of as-deposited Fe at a) low magnification and b) high magnification, c) CDF TEM image of a different region showing the distribution of nanograins, d) selected-area diffraction pattern collected from the film, and e) annular dark field STEM image. f) EELS analysis of as-deposited film showing Fe peak but no evidence of Fe oxides.

5.2.2 Qualitative Analysis of Oxidation in Water Vapor

Upon illuminating the sample with the electron beam, it was observed that the film quickly dewetted and oxidation initiated soon after. Figure 50 is a series of bright-field images showing beam-accelerated oxidation of the Fe film after the liquid layer has dewetted. A region in the middle of the view field began to oxidize, accelerated by the irradiation of the electron beam, and the evolution of this oxidation event was recorded. As can be seen, the oxidation front expanded heterogeneously and sporadically from the existing oxidized region, with oxidation fronts initiating and arresting, consuming on the order of 10's of grains in that time. A new oxidation front would then initiate, either from

the same location or another region of the previous front. The location of this reinitiation point could not be determined *a priori*, though the irregularity of the oxidation path suggests a microstructural influence. Further observation shows that the oxide is unstable, leading to dissolution of the material, suggesting a thin liquid layer may remain after exposure to the electron beam, although this could not be verified directly.

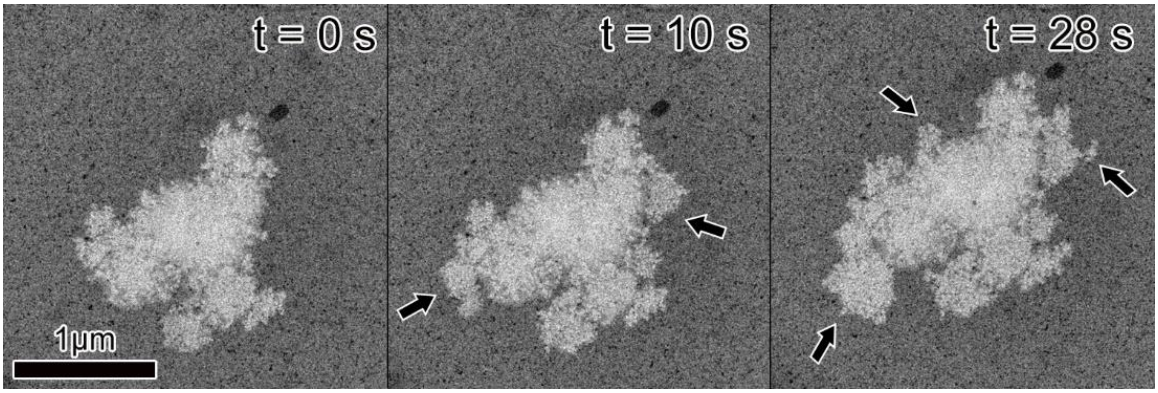

Figure 50: Time sequence from bright-field TEM videos of an oxidation event, showing propagation of the oxidation front. Arrows indicate freshly oxidized regions.

Figure 51 shows an example of the oxidation front propagation at higher magnification. Here it can be seen that the oxidation propagation occurs by discrete jumps ahead of the existing front and then backfills in as the front catches up. The reason for this behavior is currently unknown. It could be that these sites have some microstructural feature (e.g. grain boundary energy) or surface artifact that is more susceptible to the oxidation, making them easier initiation points. Then, as these sites dissolve, a sufficient amount of reactive species are created to facilitate the neighboring areas to be oxidized. However, without detailed information on the local microstructural characteristics, further study will be required. Interactions of the electron beam with water molecules are known to generate positive and negative ions, free radicals, and excited molecules, resulting in

changes in the environment chemistry and pH. These interactions have been shown to accelerate oxidation processes during LC-TEM observations in aqueous environments [58, 62], and as radiolytic species can be generated during electron beam interactions with water vapor [75], we expect the electron beam to have a similar accelerating effect in this work.

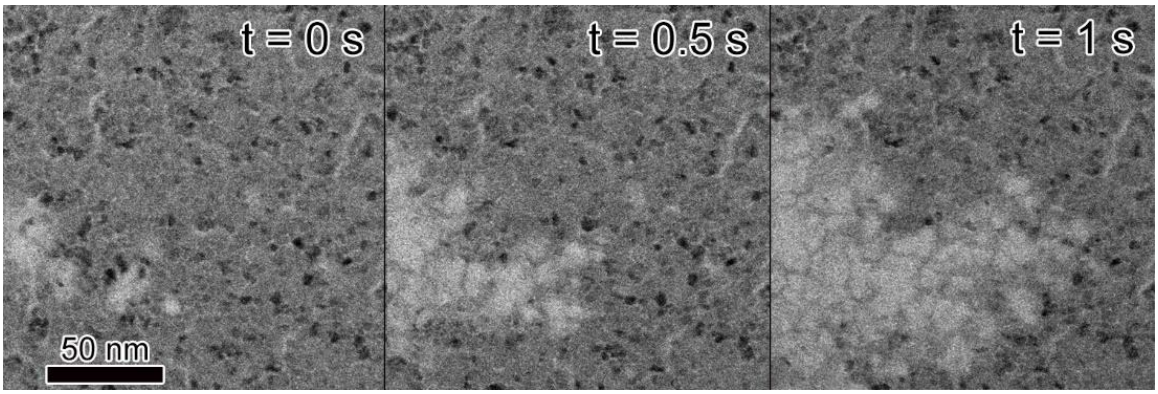

Figure 51: Time sequence from bright-field video of an oxidation event showing discrete jump and backfill behavior of the oxidation front.

5.2.3 Quantitative Analysis of Oxidation Behavior

By taking an image difference between frames, the newly oxidized region can be isolated and, by filtering and thresholding the difference image, the exact area of the oxidized region determined. An example of this is shown in Figure 52. Similar to what was seen in Figure 51, the oxidation front propagated by a discrete jump. The analysis showed that, treating the problem as two-dimensional, 180 nm^2 was consumed by the jump, correlating to a diameter of approximately 15 nm. The similarity in size of the oxidized region and the average grain size suggests that the front propagation behavior is influenced by the film microstructure.

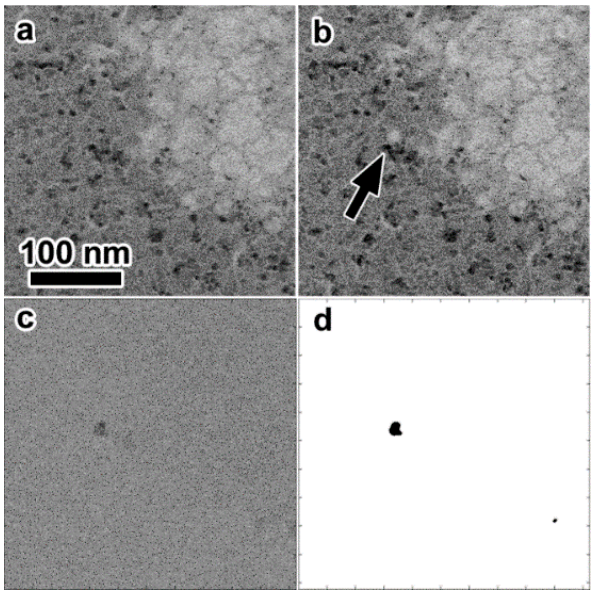

Figure 52: Image analysis of a jump event during the oxidation front propagation: a) prior to jump event, b) highlighting the jump, c) image difference, and d) thresholded image difference. Frames a and b are separated by 0.01 s.

The type of analysis shown in Figure 52 above can be extended into an automated sequential thresholding routine, which allows entire video datasets to be rapidly analyzed to track the local oxidation rate and reveal the oxidation front morphology. In the automated process, the intensity of multiple images is averaged together and filtered using a lowpass-highpass filter to reduce noise. The image difference between a specified number of frames is taken and the resultant image difference is binarized using a fixed threshold value. The binarized image can be used to extract the total oxidized area as well as the current-frame oxidation rate. To further reduce noise effects, a minimum object size is set and all objects below this threshold that are detected as oxidized are filtered out.

This approach was used to investigate the influence of electron dose rate on the oxidation rate and behavior. In these experiments, the exact dose rate was not recorded, but it can be estimated using values from additional experiments at similar operating

conditions. Two events at very different magnifications and dose rates were recorded: the higher dose rate event was on the order of 1500 $e^{-}nm^{-2}s^{-1}$ (Fig.53a-d,i) and the lower dose rate event was approximately 500 $e^{-}nm^{-2}s^{-1}$ (Fig. 53e-h,j). In Figure 53, the accumulated newly oxidized area at two different times is shown for each magnification. Image processing parameters were optimized by manually comparing binarized images with the micrographs. In this case, 5 frames were averaged together, and the image differences were taken 25 frames apart. As the image differencing only shows newly oxidized area, the upper-right portion of Figure 53f and h, which was corroded prior to the start of observation, is not detected in the image differences and remains black. Only new oxidation events during observation appear in the analysis.

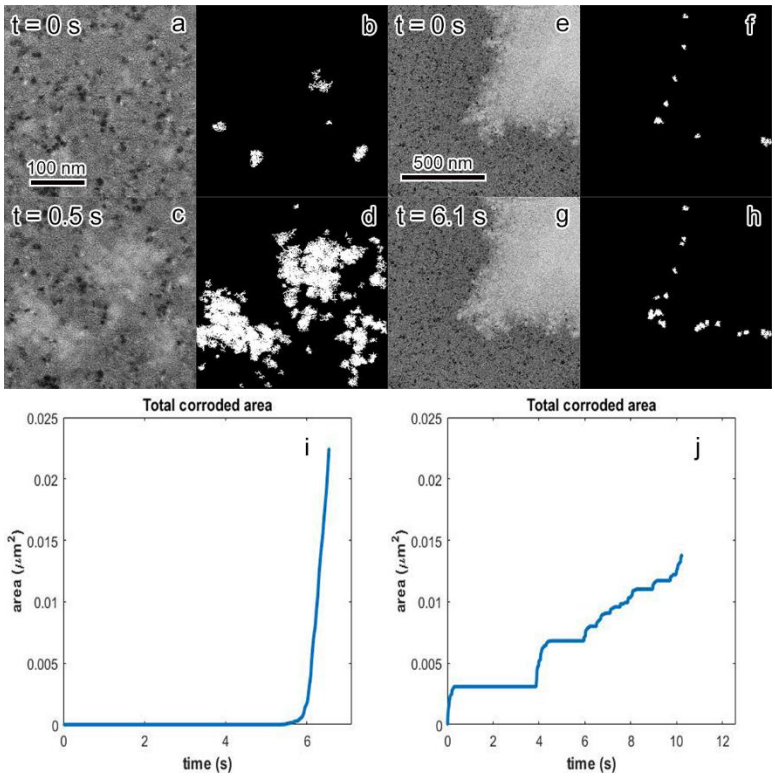

Figure 53: Bright field images captured from video showing the initiation and expansion of the oxidation front for a higher dose rate event (a,c) and lower dose rate event (e,g). Associated binarized image differences showing the newly oxidized area over the 0.5 s time span (b,d) and the 6.1 s time span for the low dose rate (f,h). Total corroded area as a function of time for the higher dose rate event (i) and lower dose rate event (j) which shows arresting and reinitiation behavior that is not seen in the higher dose rate event.

Clearly, the oxidation rate is higher at higher dose rate. The dose rate also seems to affect the sizes of the oxidation jump sites. The average size of the sites was measured by examining several frames of the difference images to find where jump sites occurred. The jump sites were defined for the lower dose rate case as the stable size of the oxidized area before the oxidation paused and reinitiated. Since the higher dose rate case did not exhibit pauses in the oxidation, the jump sites were given approximately one second to stabilize after first appearing before measurement. This was to ensure that an actual oxidation jump was occurring. For each case, several frames were examined to find ten jump sites to be

measured and the average diameter was calculated. At the higher dose rate, the average diameter of the oxidation jump sites was approximately 19 nm +/- 1 nm. As was the case in Figure 51, this is quite similar to the film grain size. However, at the lower dose rate, the size of the jump sites was slightly larger than the average grain size. During the experiment shown in Figure 53e-h, the average diameter was approximately 27 nm +/- 3 nm. Further investigation at more dose rates will provide additional insight to this effect.

In addition to allowing the size of the oxidation jump sites to be compared, this automated sequential thresholding also tracks the local oxidation rate. This can reveal differences in both kinetics and mechanisms, as shown in Figure 53i and j. At the lower dose rate, the pattern of pausing and reinitiating (as in Figure 50) is again observed. However, the higher dose rate event does not show this behavior but instead oxidizes steadily and more rapidly (about 20 times faster) than the lower dose rate case. Local beam-induced heating was not measured in these experiments but should have a negligible impact on the observed behavior. Thus we demonstrate that the type of analysis in Figure 53i and j allows us to distinguish differences in both kinetics and oxidation behavior. To further investigate the quantitative effects of dose rate on oxidation initiation size and rate, additional experiments at a series of magnifications and recorded dose rates will be performed in a future study.

Observations were also made in diffraction space, providing insight into the crystallographic evolution of the film during the corrosion process. The beam was moved to an unoxidized area and recording of the diffraction patterns was initiated. The dose rate was similar to that for the high dose rate event depicted in Figure 53 (on the order of 1500 $e^{-}nm^{-2}s^{-1}$). Image analysis of the diffraction patterns (Fig. 54) shows that the film is initially

composed of polycrystalline Fe with no preferred texture. As the beam-accelerated corrosion process progressed, the sharpness of the diffraction rings decreased, suggesting a reduction in crystallinity; this is readily apparent from the loss of higher-order ring patterns in Figure 54b. Signal detection algorithms can be used to isolate diffraction peaks from byproducts during the evolution of the film; however, it is often beneficial to have a narrow regime in which to search. The radial integration analysis described below is one way to refine the search field for signal detection.

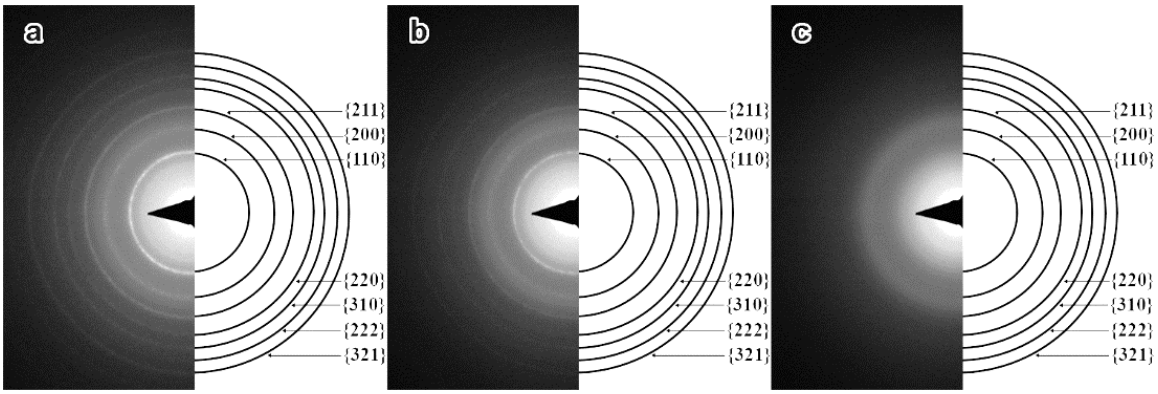

Figure 54: Time sequence of diffraction patterns at t = 23 s (a), 26 s (b), and 33 s (c), showing phase change at one location as the corrosion proceeds.

Using approximately 1500 diffraction patterns corresponding to the dissolution event shown in Figure 54, crystallographic evolution was tracked to extract information using a radial integration-based approach (Fig. 55). Figure 55a shows the radial integration of the intensity of a diffraction pattern prior to the onset of oxidation, with peaks associated with diffraction from α-Fe clearly evident. This radial integration approach was automated and applied to all 1,500 diffraction patterns, providing a quantification of the diffraction peak intensity as a function of diffraction angle (i.e. radius) and time. The variance of the diffraction intensity as a function of radius across the entire event was calculated and is

plotted in Figure 55b. Physically, this plot identifies diffraction angles at which the largest changes occur during the corrosion process. As can be seen, Bragg angles associated with α-Fe appear the largest in the plot, indicative of the dissolution process evident in Figure 54. The background intensity, which undergoes little change over the dissolution process, appears flat. Closer inspection of the variance plot can reveal information that is difficult to extract from the mean intensity plot. In this case, two subtle peaks were identified that corresponded to expected spacings for either Fe_2O_3 or Fe_3O_4 (Fig. 55b). The diffraction signal for these oxides are not readily apparent from Figure 6, showing the usefulness of the above analysis.

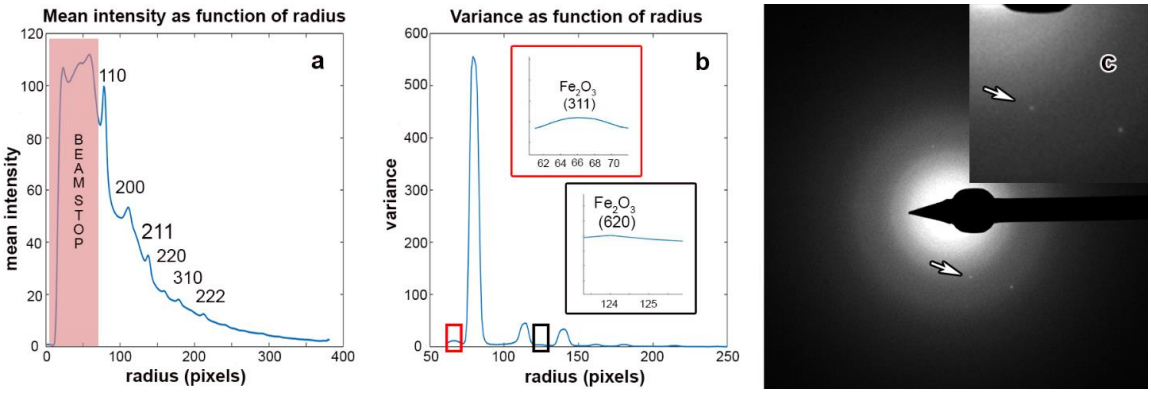

Figure 55: a-b) Radial integration and variance analysis of diffraction pattern evolution during corrosion. The six peaks corresponding to the first six Fe Bragg peaks are labeled in the mean intensity plot (a). Closer inspection of two points of the variance plot is shown in (b). The leftmost peak (red box) is shown in the upper left inset, labeled as the (311) peak of Fe_2O_3. The right peak (black box) is shown in the lower right inset, labeled as the (620) peak of Fe_2O_3. c) SAD pattern highlighting the diffraction spot associated with Fe-oxide. The spot marked by the arrow corresponds to (421) in Fe_2O_3.

Figure 55c shows the diffraction peak pattern which contributed to the peak in the variance plot associated with Fe-oxide. This peak was identified using a sequential adaptive change-point detection algorithm in the radial range identified in the variance plot, the

details of which can be found here [76]. The diffraction spot marked by the arrow was identified unambiguously at corresponding to the (421) peak in Fe_2O_3. However, the spot not marked by an arrow could be the (533) peak in either Fe_2O_3 or Fe_3O_4 (the difference is sub-angstrom). This confirms that Fe_2O_3 is a byproduct in the experiment but does not rule out the possible presence of Fe_3O_4. This highlights the importance of combining both radial intensity analysis with signal detection algorithms to identify the reaction byproducts. Radial intensity analysis alone may not be able to make unambiguous identification, but it can narrow down the field to reduce the load for the signal detection.

CHAPTER 6. SUMMARY AND CONCLUSIONS

6.1.1 Mesoscale Investigations

The results in this work contribute to the understanding of the impact of microstructure on pitting corrosion in the AA5083 system. A toolset combining rapid microstructural characterization with automated image analysis was used to investigate grain orientation, intermetallic particle proximity, grain boundary proximity, and local GND density with regards to their effect on pitting. This work highlights the usefulness of such analysis in developing P-S-P relations in this and other material systems. Specific observations include:

- Grain orientation did not appear to strongly affect pit initiation sites, as the texture of the pitted points was very similar to that of the initial texture.
- Increased pitting occurred near noble intermetallic particles, sharply dropping off after about 10 microns. This is in agreement with observed galvanic effects of intermetallics. Active particles were too few to be yield extensive statistics.
- Relative pitting seemed to increase slightly at higher GND densities, although this effect was quite small compared to that of intermetallic particles.
- In this work, grain boundary proximity did not show a clear correlation with relative pitting. Future refinement that categorizes different types of grain boundaries is needed.

By combining rapid microstructural characterization from EBSD with automated image analysis, it is possible to develop first-order correlations between multiple

microstructural features and pitting initiation in a statistical manner. Furthermore, these methods can be applied to corrosion in other materials systems or to different damage phenomena, such as void formation in irradiated materials.

6.1.2 Nanoscale Investigations

The results presented in this work show the developing use of *in situ* liquid cell electron microscopy to study oxidation in water-vapor environments, as well as the need for automated image analysis routines to extract the maximum information from the large data sets created by such experiments. Specific observations include:

- The electron dose rate had a significant impact on the oxidation rate, with higher dose rate leading to more rapid oxidation.
- The electron dose rate influenced the oxidation behavior, with the low dose rate events exhibiting a pattern of pausing and resuming whereas the high dose rate events exhibited steady oxidation.
- Radial integration analysis was used to refine the search field for a sequential adaptive change point algorithm that identified diffraction peaks associated with corrosion byproduct.

By coupling high-speed imaging and specialized LC-TEM holders, it is possible to obtain information on local oxidation rates, oxidation behavior, and byproducts. This holds great promise for developing the understanding of local corrosion processes. Future opportunities could include extending the analysis to track the fractality of the oxidation front, which is of interest in cellular automata modeling [77, 78]. The possibility of using scanning nanobeam diffraction [79] or precession electron diffraction [80] in combination

with liquid cell to provide more localized diffraction information and more direct correlation with local microstructure is also promising[74].

6.1.3 Future Work and Considerations

This work has investigated the corrosion behavior of materials at both the mesoscale and the nanoscale, developing analysis frameworks for the development of P-S-P relations and leveraging automated image analysis to extract crucial information from rich data sets. It has laid the groundwork for future developments and refinements and the application of the methods here to other systems.

At the mesoscale, there are several areas that show potential for further investigation. First, adapting the region of interest to incorporate the study of active intermetallics will build a more complete picture of how these secondary phase particles influence pitting. The strongest microstructural influence in this work was for noble intermetallics, so galvanic effects may also play a strong role in the pitting behaviour near active intermetallics. The region of interest can either be enlarged to incorporate more active particles or it can be reduced and centered on the particle itself (having one active particle per region).

Another refinement of the analysis would be to differentiate between different kinds of grain boundary. Separating low-angle, high-angle, and coincident site lattice boundaries would likely lead to clearer correlations because these could each affect pit initiation differently. Additionally, higher order correlations could be developed by analysing, for example, GND density gradients rather than the magnitude of the GND density. Alternatively, spatial statistics could be used to study the pitting density in a region as a

function of the distribution of active and noble particles, making use of two-point correlations. These kinds of higher order correlations provide further insight into the interplay of various microstructural features.

Another prospect is to use machine learning methods to classify different intermetallic particles based on their corrosion behavior, sorting out particles that have pitting in the vicinity, particles that have trenching around them, and particles that have both or neither of those behaviors. Classifying large numbers of particles into such categories and identifying their chemical composition with EDS could give a statistical prediction of the expected corrosion behavior based on the composition of the intermetallic.

At the nanoscale, the next step is to repeat the LC-TEM experiments for AA5083 thin films. Investigations both with and without potentiostatic control would provide more insight into the early stages of corrosion initiation. Furthermore, both sensitized and unsensitized samples could be studied to examine the effect of β phase on corrosion pathways and propagation kinetics. Transmission Kikuchi diffraction (also called transmission EBSD) provides detailed characterization of grain boundary character for thin samples, facilitating the study of IGC in an LC-TEM environment. Regardless of experimental design, continued development of automated processing and analysis will be instrumental in better understanding corrosion behavior.

REFERENCES

1. Gupta, A., et al., *Structure–property linkages using a data science approach: Application to a non-metallic inclusion/steel composite system.* Acta Materialia, 2015. **91**: p. 239-254.

2. Choudhury, A., et al., *Quantification and classification of microstructures in ternary eutectic alloys using 2-point spatial correlations and principal component analyses.* Acta Materialia, 2016. **110**: p. 131-141.

3. Fast, T., et al., *Microstructure taxonomy based on spatial correlations: Application to microstructure coarsening.* Acta Materialia, 2016. **108**: p. 176-185.

4. Jain, A., et al., *Commentary: The Materials Project: A materials genome approach to accelerating materials innovation.* APL Materials, 2013. **1**(1): p. 011002.

5. Ji, J., et al., *Prediction of stress concentration factor of corrosion pits on buried pipes by least squares support vector machine.* Engineering Failure Analysis, 2015. **55**: p. 131-138.

6. Koch, G., et al., *International measures of prevention, application, and economics of corrosion technologies study.* NACE International IMPACT Report, 2016.

7. Adams, B.L., S. Kalidindi, and D.T. Fullwood, *Microstructure sensitive design for performance optimization*. 2012: Butterworth-Heinemann.

8. Pantleon, W., *Resolving the geometrically necessary dislocation content by conventional electron backscattering diffraction.* Scripta Materialia, 2008. **58**(11): p. 994-997.

9. Ruggles, T.J., et al., *The effect of length scale on the determination of geometrically necessary dislocations via EBSD continuum dislocation microscopy.* Ultramicroscopy, 2016. **164**: p. 1-10.

10. de Jonge, N. and F.M. Ross, *Electron microscopy of specimens in liquid.* Nature Nanotechnology, 2011. **6**: p. 695.

11. Ross, F.M., *Opportunities and challenges in liquid cell electron microscopy.* Science, 2015. **350**(6267).

12. Key, J.W., et al., *Investigating local oxidation processes in Fe thin films in a water vapor environment by in situ liquid cell TEM.* Ultramicroscopy, 2020. **209**: p. 112842.

13. Jones, D.A., *Principles and prevention of corrosion*. 1992: Macmillan.

14. Steels, A. *Atlas Tech Note No. 7 Galvanic Corrosion*. 2010; Available from: http://www.atlassteels.com.au/documents/TN7-Galvanic_Corrosion_rev_Aug_2010.pdf.

15. Mansfeld, F. and J.V. Kenkel, *Galvanic corrosion of Al alloys—III. The effect of area ratio.* Corrosion Science, 1975. **15**(4): p. 239-250.

16. Oldfield, J.W., *Electrochemical theory of galvanic corrosion*, in *Galvanic Corrosion*. 1988, ASTM International.

17. Szklarska-Smialowska, Z., *Pitting corrosion of aluminum.* Corrosion Science, 1999. **41**(9): p. 1743-1767.

18. Frankel, G., *Pitting corrosion of metals a review of the critical factors.* Journal of the Electrochemical Society, 1998. **145**(6): p. 2186-2198.

19. Zaid, B., et al., *Effects of pH and chloride concentration on pitting corrosion of AA6061 aluminum alloy.* Corrosion Science, 2008. **50**(7): p. 1841-1847.

20. Brunner, J.G., et al., *Localized corrosion of ultrafine-grained Al–Mg model alloys.* Electrochimica Acta, 2010. **55**(6): p. 1966-1970.

21. Kus, E., et al., *A Comparison of the Corrosion Behavior of Nanocrystalline and Conventional Al 5083 Samples.* CORROSION, 2006. **62**(2): p. 152-161.

22. Sikora, E., X.J. Wei, and B.A. Shaw, *Corrosion Behavior of Nanocrystalline Bulk Al-Mg-Based Alloys.* CORROSION, 2004. **60**(4): p. 387-398.

23. Chung, M.-K., et al., *Effect of the number of ECAP pass time on the electrochemical properties of 1050 Al alloys.* Materials Science and Engineering: A, 2004. **366**(2): p. 282-291.

24. Ralston, K.D., N. Birbilis, and C.H.J. Davies, *Revealing the relationship between grain size and corrosion rate of metals.* Scripta Materialia, 2010. **63**(12): p. 1201-1204.

25. Davenport, A.J., et al., *Intergranular Corrosion and Stress Corrosion Cracking of Sensitised AA5182.* Materials Science Forum, 2006. **519-521**: p. 641-646.

26. Scotto D'Antuono, D., et al., *Grain boundary misorientation dependence of β phase precipitation in an Al–Mg alloy.* Scripta Materialia, 2014. **76**: p. 81-84.

27. Kaigorodova, L.I., *The Effect of Grain-Boundary Structure Formation on β-Precipitation in Aged Al-Mg Alloys.* Materials Science Forum, 1998. **294-296**: p. 477-480.

28. Zhao, Y., et al., *The role of grain boundary plane orientation in the β phase precipitation of an Al–Mg alloy.* Scripta Materialia, 2014. **89**: p. 49-52.

29. Yan, J., et al., *Improve sensitization and corrosion resistance of an Al-Mg alloy by optimization of grain boundaries.* Scientific Reports, 2016. **6**: p. 26870.

30. Talianker, M. and B. Cina, *Retrogression and reaging and the role of dislocations in the stress corrosion of 7000-type aluminum alloys.* Metallurgical Transactions A, 1989. **20**(10): p. 2087-2092.

31. Takayama, Y., K. Nohara, and H. Kato. *Influence of Crystallographic Orientation on Corrosion Behaveor of 5N Purity Aluminum*. in *Proceeding of the 12th International Conference on Aluminum Alloys*. 2010.

32. Tan, L. and T.R. Allen, *Effect of thermomechanical treatment on the corrosion of AA5083.* Corrosion Science, 2010. **52**(2): p. 548-554.

33. Yasakau, K.A., et al., *Role of intermetallic phases in localized corrosion of AA5083.* Electrochimica Acta, 2007. **52**(27): p. 7651-7659.

34. Donatus, U., et al., *Corrosion pathways in aluminium alloys.* Transactions of Nonferrous Metals Society of China, 2017. **27**(1): p. 55-62.

35. Cavanaugh, M., et al., *Electrochemical characterization of intermetallic phases common to aluminum alloys as a function of solution temperature.* Journal of The Electrochemical Society, 2014. **161**(12): p. C535-C543.

36. King, P.C., et al., *FIB/SEM study of AA2024 corrosion under a seawater drop: Part I.* Corrosion Science, 2011. **53**(3): p. 1086-1096.

37. Ralston, K., et al., *Role of nanostructure in pitting of Al–Cu–Mg alloys.* Electrochimica acta, 2010. **55**(27): p. 7834-7842.

38. Minoda, T. and H. Yoshida, *Effect of grain boundary characteristics on intergranular corrosion resistance of 6061 aluminum alloy extrusion.* Metallurgical and Materials Transactions A, 2002. **33**(9): p. 2891-2898.

39. Shimada, M., et al., *Optimization of grain boundary character distribution for intergranular corrosion resistant 304 stainless steel by twin-induced grain boundary engineering.* Acta Materialia, 2002. **50**(9): p. 2331-2341.

40. Hockauf, M., et al., *Mechanical properties and corrosion behaviour of ultrafine-grained AA6082 produced by equal-channel angular pressing.* Journal of Materials Science, 2008. **43**(23): p. 7409.

41. Shahryari, A., J.A. Szpunar, and S. Omanovic, *The influence of crystallographic orientation distribution on 316LVM stainless steel pitting behavior.* Corrosion Science, 2009. **51**(3): p. 677-682.

42. Böhni, H. and H.H. Uhlig, *Environmental factors affecting the critical pitting potential of aluminum.* Journal of the Electrochemical Society, 1969. **116**(7): p. 906-910.

43. Shao, M., et al., *A study on pitting corrosion of aluminum alloy 2024-T3 by scanning microreference electrode technique.* Materials Science and Engineering: A, 2003. **344**(1): p. 323-327.

44. Chen, J., et al., *Effect of precipitate state on the stress corrosion behavior of 7050 aluminum alloy.* Materials Characterization, 2016. **114**: p. 1-8.

45. Searles, J.L., P.I. Gouma, and R.G. Buchheit, *Stress corrosion cracking of sensitized AA5083 (Al-4.5Mg-1.0Mn).* Metallurgical and Materials Transactions A, 2001. **32**(11): p. 2859-2867.

46. Lathabai, S. and P.G. Lloyd, *The effect of scandium on the microstructure, mechanical properties and weldability of a cast Al–Mg alloy.* Acta Materialia, 2002. **50**(17): p. 4275-4292.

47. Oguocha, I.N.A., O.J. Adigun, and S. Yannacopoulos, *Effect of sensitization heat treatment on properties of Al–Mg alloy AA5083-H116.* Journal of Materials Science, 2008. **43**(12): p. 4208-4214.

48. Birbilis, N., et al., *Quantification of Sensitization in AA5083-H131 via Imaging Ga-Embrittled Fracture Surfaces.* CORROSION, 2012. **69**(4): p. 396-402.

49. Gao, J. and D.J. Quesnel, *Enhancement of the Stress Corrosion Sensitivity of AA5083 by Heat Treatment.* Metallurgical and Materials Transactions A, 2011. **42**(2): p. 356-364.

50. Carroll, M., et al., *Effects of Zn additions on the grain boundary precipitation and corrosion of Al-5083.* Scripta materialia, 2000. **42**(4): p. 335-340.

51. Jones, R.H., J.S. Vetrano, and C. Windisch Jr, *Stress corrosion cracking of Al-Mg and Mg-Al alloys.* Corrosion, 2004. **60**(12): p. 1144-1154.

52. Goswami, R., et al., *Precipitation behavior of the ß phase in Al-5083.* Materials Science and Engineering: A, 2010. **527**(4-5): p. 1089-1095.

53. Goswami, R. and R.L. Holtz, *Transmission electron microscopic investigations of grain boundary beta phase precipitation in Al 5083 aged at 373 K (100 C).* Metallurgical and Materials Transactions A, 2013. **44**(3): p. 1279-1289.

54. Yan, J. and A.M. Hodge, *Study of β precipitation and layer structure formation in Al 5083: The role of dispersoids and grain boundaries.* Journal of Alloys and Compounds, 2017. **703**: p. 242-250.

55. Wiliams, D.B. and C.B. Carter, *Transmission electron microscopy.* III Imaging, 1996.

56. Williamson, M.J., et al., *Dynamic microscopy of nanoscale cluster growth at the solid–liquid interface.* Nature Materials, 2003. **2**: p. 532.

57. Gu, M., et al., *Demonstration of an Electrochemical Liquid Cell for Operando Transmission Electron Microscopy Observation of the Lithiation/Delithiation Behavior of Si Nanowire Battery Anodes.* Nano Letters, 2013. **13**(12): p. 6106-6112.

58. Chee, S.W., et al., *Studying localized corrosion using liquid cell transmission electron microscopy.* Chemical Communications, 2015. **51**(1): p. 168-171.

59. Chee, S.W., et al., *Metastable Structures in Al Thin Films Before the Onset of Corrosion Pitting as Observed using Liquid Cell Transmission Electron Microscopy.* Microscopy and Microanalysis, 2014. **20**(2): p. 462-468.

60. Chee, S.W., et al., *Capturing Dynamics in Liquids with High-Speed CMOS Cameras-Opportunities and Challenges.* Microscopy and Microanalysis, 2017. **23**(S1): p. 860-861.

61. *http://www.protochips.com/products/poseidon-select/.*

62. Gross, D., et al., *In Situtem Observations of Corrosion in Nanocrystalline Fe Thin Films.* Processing, Properties, and Design of Advanced Ceramics and Composites II: Ceramic Transactions, 2016. **261**: p. 327-338.

63. McCafferty, E., *Sequence of steps in the pitting of aluminum by chloride ions.* Corrosion Science, 2003. **45**(7): p. 1421-1438.

64. Pride, S., J. Scully, and J. Hudson, *Metastable pitting of aluminum and criteria for the transition to stable pit growth.* Journal of the Electrochemical Society, 1994. **141**(11): p. 3028-3040.

65. Frankel, G., et al., *On the Pitting Resistance of Sputter‐Deposited Aluminum Alloys.* Journal of the Electrochemical Society, 1993. **140**(8): p. 2192-2197.

66. Meng, G., et al., *Effect of microcrystallization on pitting corrosion of pure aluminium.* Corrosion Science, 2009. **51**(9): p. 2151-2157.

67. Brewick, P.T., et al., *Microstructure-sensitive modeling of pitting corrosion: effect of the crystallographic orientation.* Corrosion Science, 2017. **129**: p. 54-69.

68. Mostaed, E., et al., *Microstructure, texture evolution, mechanical properties and corrosion behavior of ECAP processed ZK60 magnesium alloy for biodegradable applications.* journal of the mechanical behavior of biomedical materials, 2014. **37**: p. 307-322.

69. Foley, R., *Localized corrosion of aluminum alloys—a review.* Corrosion, 1986. **42**(5): p. 277-288.

70. Ghali, E., W. Dietzel, and K.-U. Kainer, *General and localized corrosion of magnesium alloys: a critical review.* Journal of materials engineering and performance, 2004. **13**(1): p. 7-23.

71. Jain, S., et al., *Spreading of intergranular corrosion on the surface of sensitized Al-4.4 Mg alloys: A general finding.* Corrosion Science, 2012. **59**: p. 136-147.

72. Schilling, S., et al., *Practical Aspects of Electrochemical Corrosion Measurements During In Situ Analytical Transmission Electron Microscopy (TEM) of Austenitic Stainless Steel in Aqueous Media.* Microscopy and Microanalysis, 2017. **23**(4): p. 741-750.

73. Park, J.H., et al., *In situ EC-TEM Studies of Metal Thin Film Corrosion in Liquid Solutions at Elevated Temperatures.* Microscopy and Microanalysis, 2018. **24**(S1): p. 254-255.

74. Hayden, S.C., et al., *Localized corrosion of low-carbon steel at the nanoscale.* npj Materials Degradation, 2019. **3**(1): p. 17.

75. Melton, C.E., *Radiolysis of water vapor in a wide range radiolysis source of a mass spectrometer. I. Individual and total cross sections for the production of positive ions, negative ions, and free radicals by electrons.* The Journal of Physical Chemistry, 1970. **74**(3): p. 582-587.

76. Cao, Y.Z., S.; Xie, Y.; Key, J.; Kacher, J.; Unocic, R.R.; Rouleau, C.M., *Sequential Adaptive Detection for In-Situ Transmission Electron Microscopy (TEM).* arXiv preprint, 2017. **arXiv:1710.11297**.

77. Stafiej, J., D. di Caprio, and Ł. Bartosik, *Corrosion-passivation processes in a cellular automata based simulation study.* The Journal of Supercomputing, 2013. **65**(2): p. 697-709.

78. Vautrin-Ul, C., et al., *Numerical simulations of spatial heterogeneity formation in metal Corrosion.* Corrosion Science, 2008. **50**(8): p. 2149-2158.

79. Gammer, C., et al., *Diffraction contrast imaging using virtual apertures.* Ultramicroscopy, 2015. **155**: p. 1-10.

80. Brons, J.G. and G.B. Thompson, *Orientation Mapping via Precession-Enhanced Electron Diffraction and Its Applications in Materials Science.* JOM, 2014. **66**(1): p. 165-170.